Phase-dependent polymerization isomerism in the coordination complexes of a flexible bis(β-diketonato) ligand

Manuel Imperato,[a,b,#] Alessio Nicolini,[a,#] Matteo Boniburini,[a] Silvia Gómez-Coca,[c] Eliseo Ruiz,[c] Fabio Santanni,[d] Lorenzo Sorace,[d] and Andrea Cornia[a,*]

[a]Dipartimento di Scienze Chimiche e Geologiche e UdR INSTM, Università degli Studi di Modena e Reggio Emilia, via G. Campi 103, 41125 Modena, Italy. E-mail: acornia@unimore.it

[b]Dipartimento di Scienze Fisiche, Informatiche e Matematiche, Università degli Studi di Modena e Reggio Emilia, via G. Campi 213/A, 41125 Modena, Italy

[c]Departament de Química Inorgànica i Orgànica, Institut de Química Teòrica i Computacional Universitat de Barcelona, Diagonal 645, 08028 Barcelona, Spain

[d]Dipartimento di Chimica "Ugo Schiff" e UdR INSTM, Università degli Studi di Firenze, via della Lastruccia 3, 50019 Sesto Fiorentino (FI), Italy

ELECTRONIC SUPPLEMENTARY INFORMATION

Supplementary Note 1: Details on the assignment of ^{1}H and ^{13}C NMR signals of H_2bdhb. The assignment of ^{1}H and ^{13}C chemical shifts (δ) was achieved through the combined use of E-HSQC, HMBC, and COSY 2D experiments. In the E-HSQC experiment (Figure S2), a distinction could be made between CH_2 and CH/CH_3 groups, which generate signals of different phase: positive for CH/CH_3 and negative for CH_2 groups. This confirmed the assignment of proton resonances to CH_2, CH, or CH_3 groups and allowed the individuation of carbon signals C*a* and C*c* in both tautomeric branches. Additionally, the keto-enolic pairs (H*e*, C*e*) and (H*f*, C*f*) were differentiated from the corresponding diketonic pairs based on their more intense E-HSQC signals, which reflect the higher concentration of the KE branches (Figure S3). With the E-HSQC experiment it was also possible to gain insight into the aromatic region (Figure S4). The contributions of the two tautomeric branches are revealed by the correlation of the H*h* multiplet with two different aromatic carbon peaks at 126.94 (Ch_{KE}) and 126.80 ppm (Ch_{KK}). The two well-separated H*j* pseudo-singlets at 7.14 and 7.11 ppm correlate with two distinct carbon signals at 129.24 and 129.21 ppm, assigned to the KE-KE and KE-KK forms, respectively. It is also possible to discern an additional correlation between the weak carbon signal at 129.18 ppm and a proton signal at 7.08 ppm (partially hidden by the H*h* multiplet), attributed to the KK-KK form. Similarly, the two extensively overlapping H*i* triplets centred at around 7.19 ppm correlate with two very close C*i* signals at 129.31 (KE-KE) and 129.30 ppm (KE-KK). Although a third C*i* signal attributable to the KK-KK form is distinguishable at 129.28 ppm (Figure 2), its correlation with the H*i* region could not be resolved.

These assignments were cross-checked using the intramolecular correlations found in HMBC and COSY experiments (Figures S5-S9). The HMBC spectra also allowed to assign the remaining ^{13}C signals to the quaternary carbons C*b*, C*d*, and C*g*.

Splittings like those of Cg_{KE} and Cg_{KK} signals in Figure S1 were in general more difficult to resolve in the ^{1}H spectra. However, we found that the Hc_{KE} signal has two resolvable components in CD_2Cl_2 and $CDCl_3$ (Figure S10). Deconvolution of this signal in CD_2Cl_2 afforded two components in a 4.0:1 ratio. If the majority and minority signals are assigned to the keto-enolic H*c* protons of the KE-KE and KE-KK forms, respectively, the proportion between the two forms is evaluated as 2.0:1, to be compared with the estimate 1.8:1 following from a statistical distribution of KE and KK branches (Table 1). The split Hc_{KE} signal observed in $CDCl_3$ (Figure S10) suggests that the proportion of KE-KK tautomer is lower than in CD_2Cl_2, consistent with the larger fraction of KE branches found in $CDCl_3$ (Table 1).

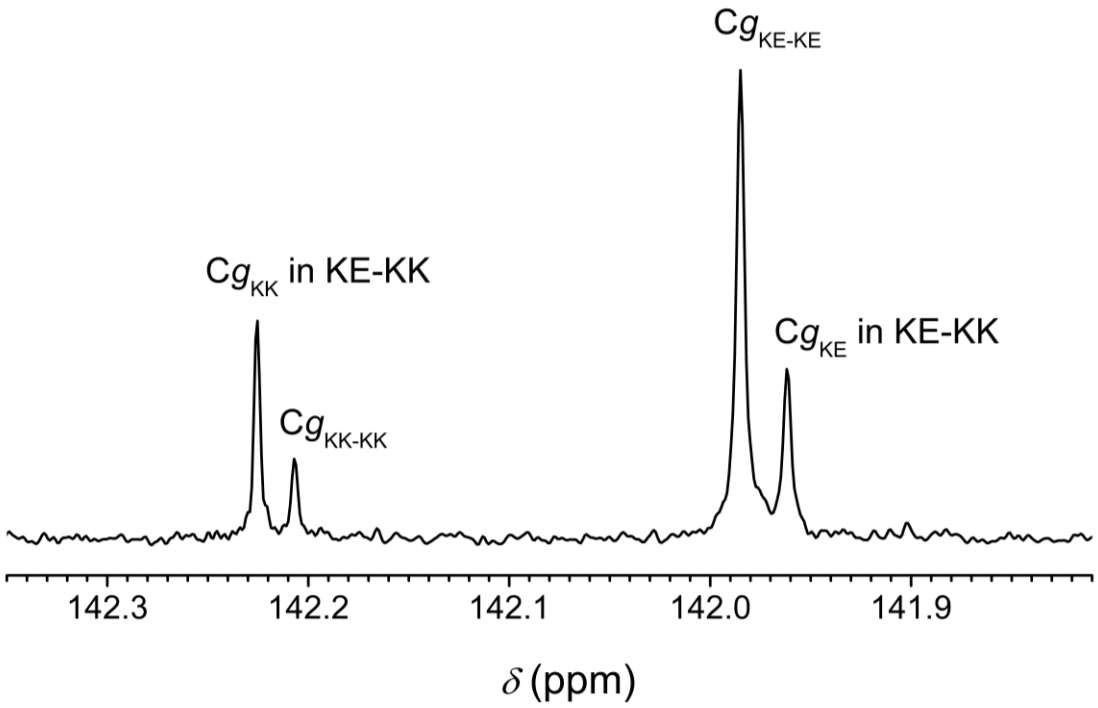

Figure S1. ^{13}C NMR spectrum of H_2bdhb in acetone-d_6 for δ = 142.3–141.9 ppm, corresponding to the C*g* region (150.90 MHz, 298 K); processing parameters (TopSpin 4.3.0[1]): SI = 2·TD, LB = 0.30 Hz.

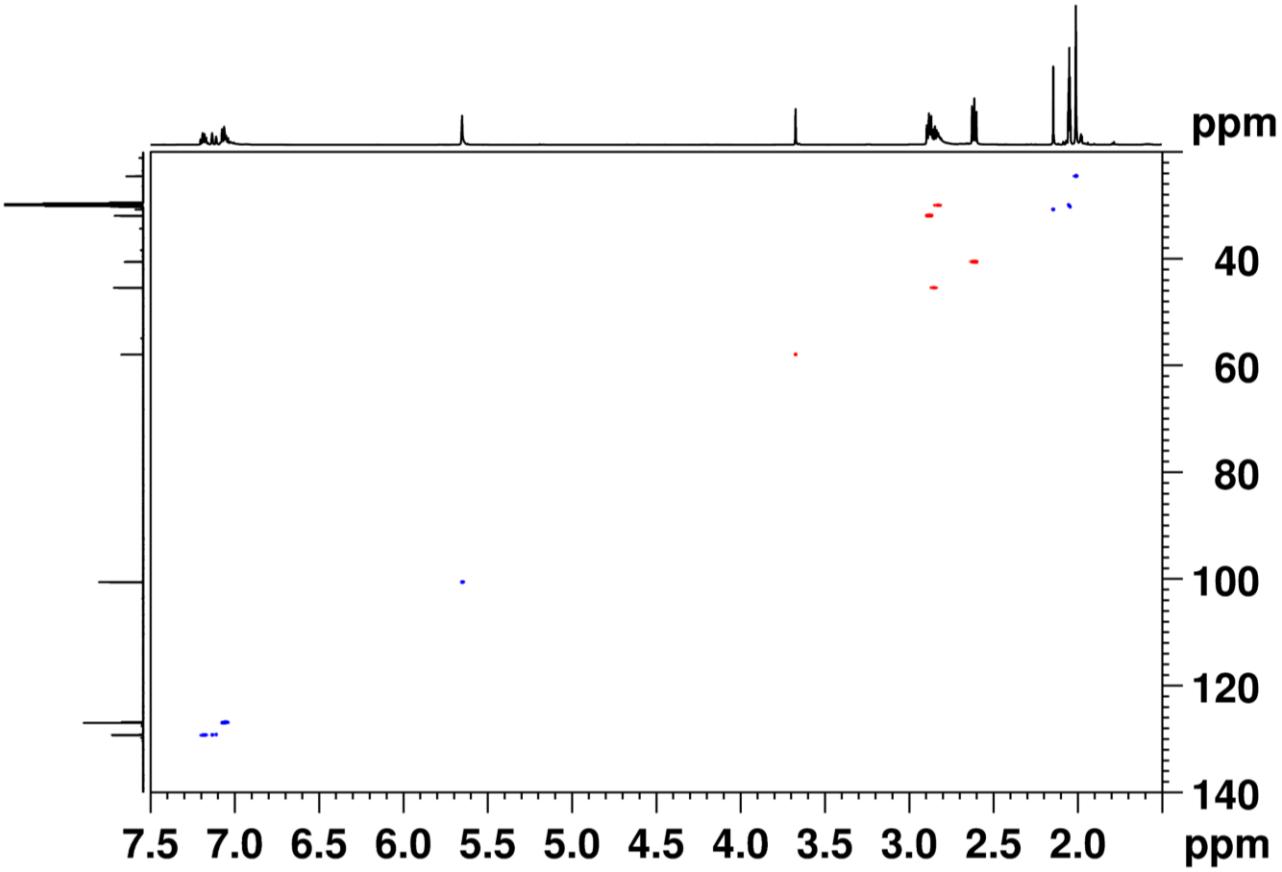

Figure S2. ^{1}H–^{13}C E-HSQC spectrum of H_2bdhb in acetone-d_6 for δ_H = 7.50–1.50 ppm and δ_C = 140–20 ppm (298 K, 600.13 MHz for F2, 150.90 MHz for F1). The cross peaks indicate the ^{1}H–^{13}C coupling (F2, F1). Color code: blue = positive phase, red = negative phase. Processing parameters (TopSpin 4.3.0[1]) for F2 (x axis): SI = 2·TD, LB = 1.00 Hz. Processing parameters for F1 (y axis): SI = 2·TD, LB = 0.30 Hz.

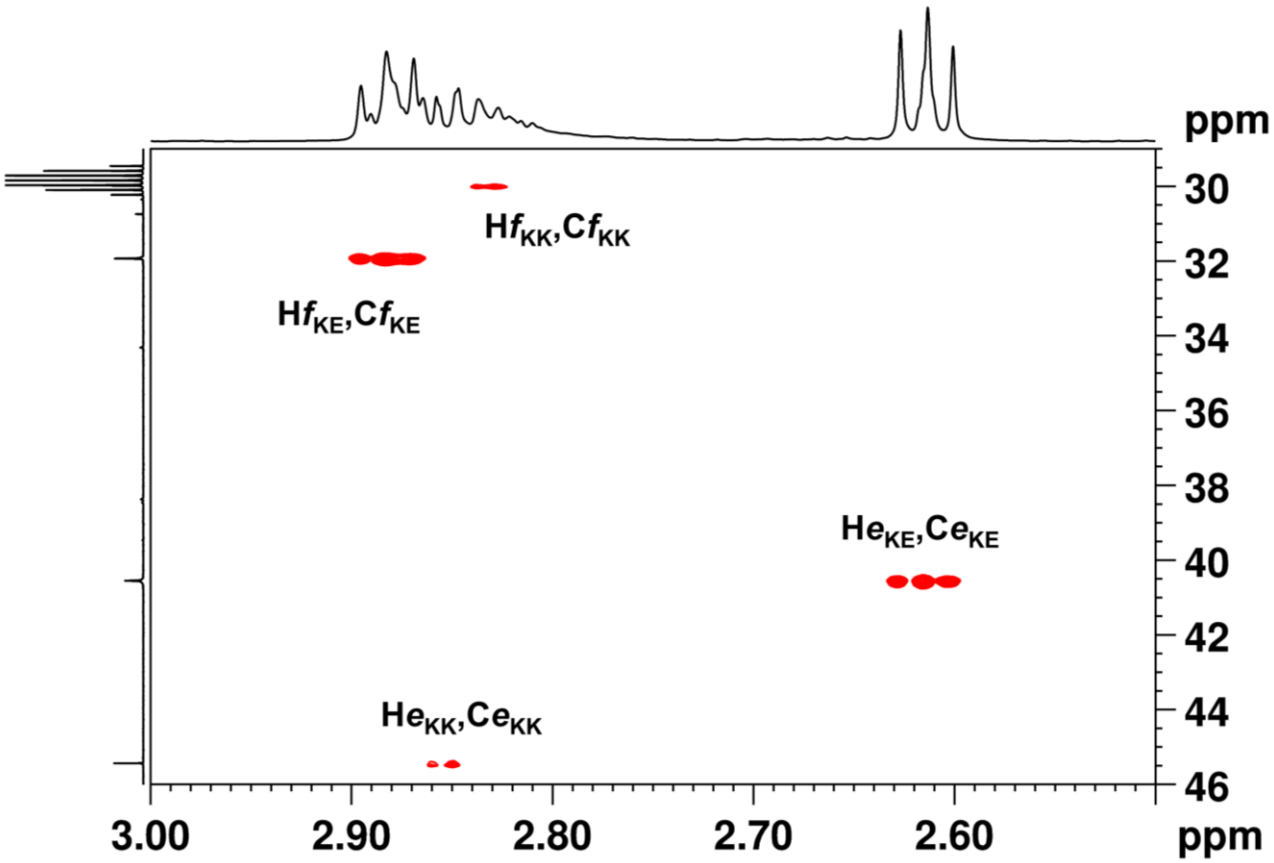

Figure S3. ^{1}H–^{13}C E-HSQC spectrum of H_2bdhb in acetone-d_6 for δ_H = 3.00–2.50 ppm and δ_C = 46–29 ppm (298 K, 600.13 MHz for F2, 150.90 MHz for F1). The labelling of the cross-peaks indicates the ^{1}H–^{13}C coupling (F2, F1). Processing parameters (TopSpin 4.3.0[1]) for F2 (x axis): SI = 2·TD, LB = 1.00 Hz. Processing parameters for F1 (y axis): SI = 2·TD, LB = 0.30 Hz.

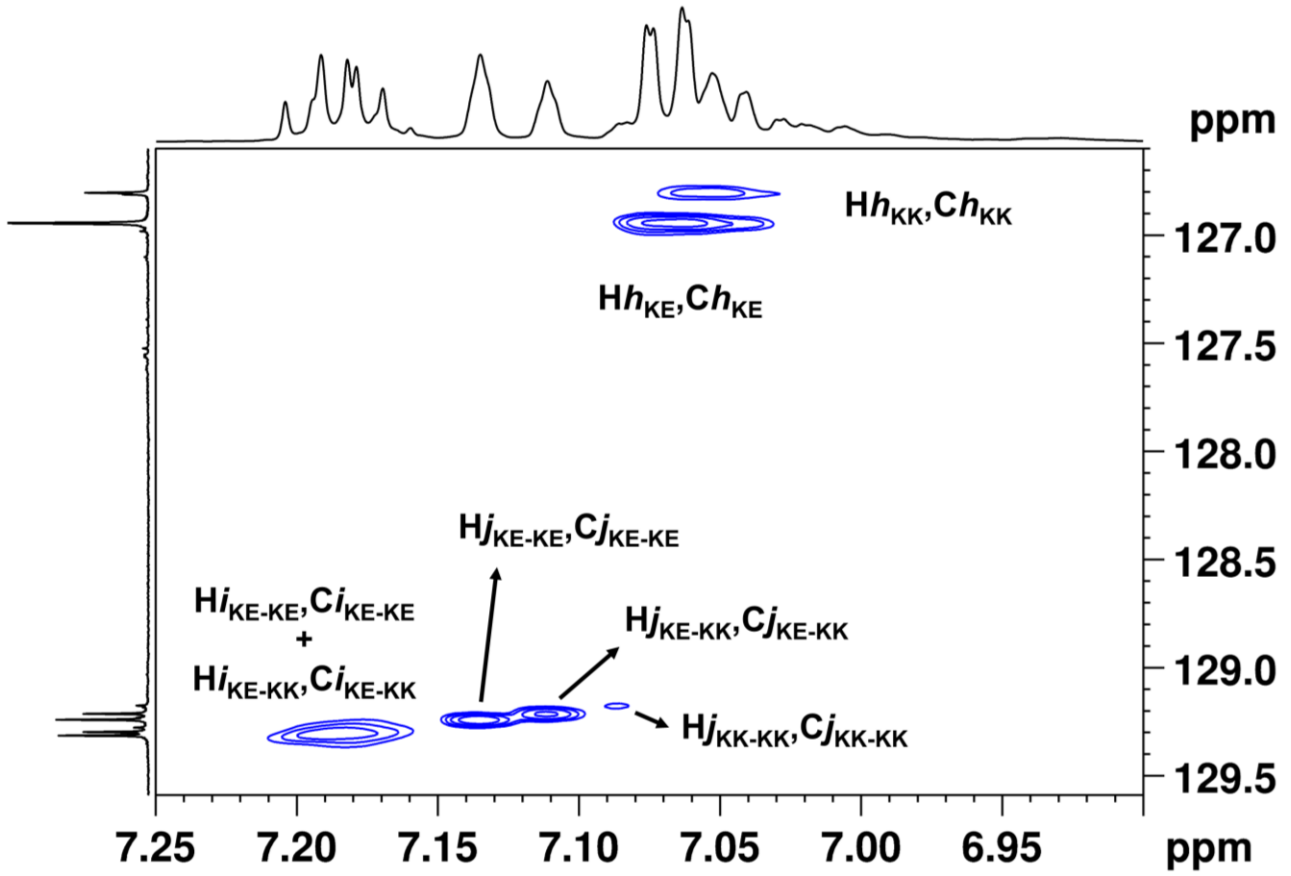

Figure S4. ^{1}H–^{13}C E-HSQC spectrum of H_2bdhb in acetone-d_6 for δ_H = 7.30–7.00 ppm and δ_C = 129.5–126.5 ppm (298 K, 600.13 MHz for F2, 150.90 MHz for F1). The labelling of the cross-peaks indicates the ^{1}H–^{13}C coupling (F2, F1). Processing parameters (TopSpin 4.3.0[1]) for F2 (x axis): SI = 2·TD, LB = 1.00 Hz. Processing parameters for F1 (y axis): SI = 2·TD, LB = 0.30 Hz.

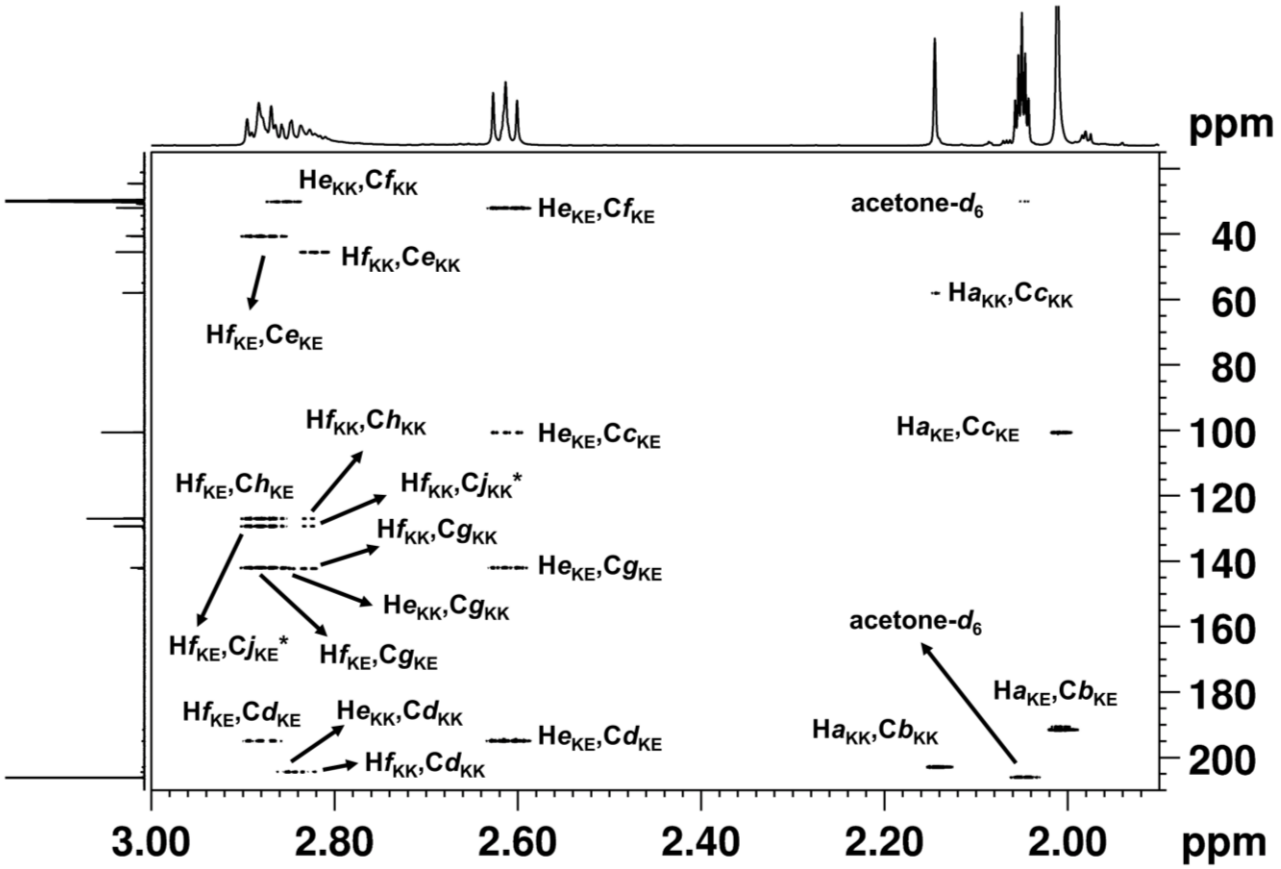

Figure S5. ^{1}H–^{13}C HMBC spectrum of H_2bdhb in acetone-d_6 for δ_H = 3.00–1.90 ppm and δ_C = 210–15 ppm (298 K, 600.13 MHz for F2, 150.90 MHz for F1). The labelling of the cross-peaks indicates the ^{1}H–^{13}C coupling (F2, F1). Processing parameters (TopSpin 4.3.0[1]) for F2 (x axis): SI = TD, LB = 1.00 Hz. Processing parameters for F1 (y axis): SI = 2·TD, LB = 0.30 Hz. The asterisk on a carbon label indicates that it is not possible to differentiate the cross peaks arising from the different tautomers because their ^{13}C signals are too close to each other. For this reason, the label Cj_{KE}* stands for both C$j_{KE\text{-}KE}$ and C$j_{KE\text{-}KK}$, and the label Cj_{KK}* stands for both C$j_{KE\text{-}KK}$ and C$j_{KK\text{-}KK}$.

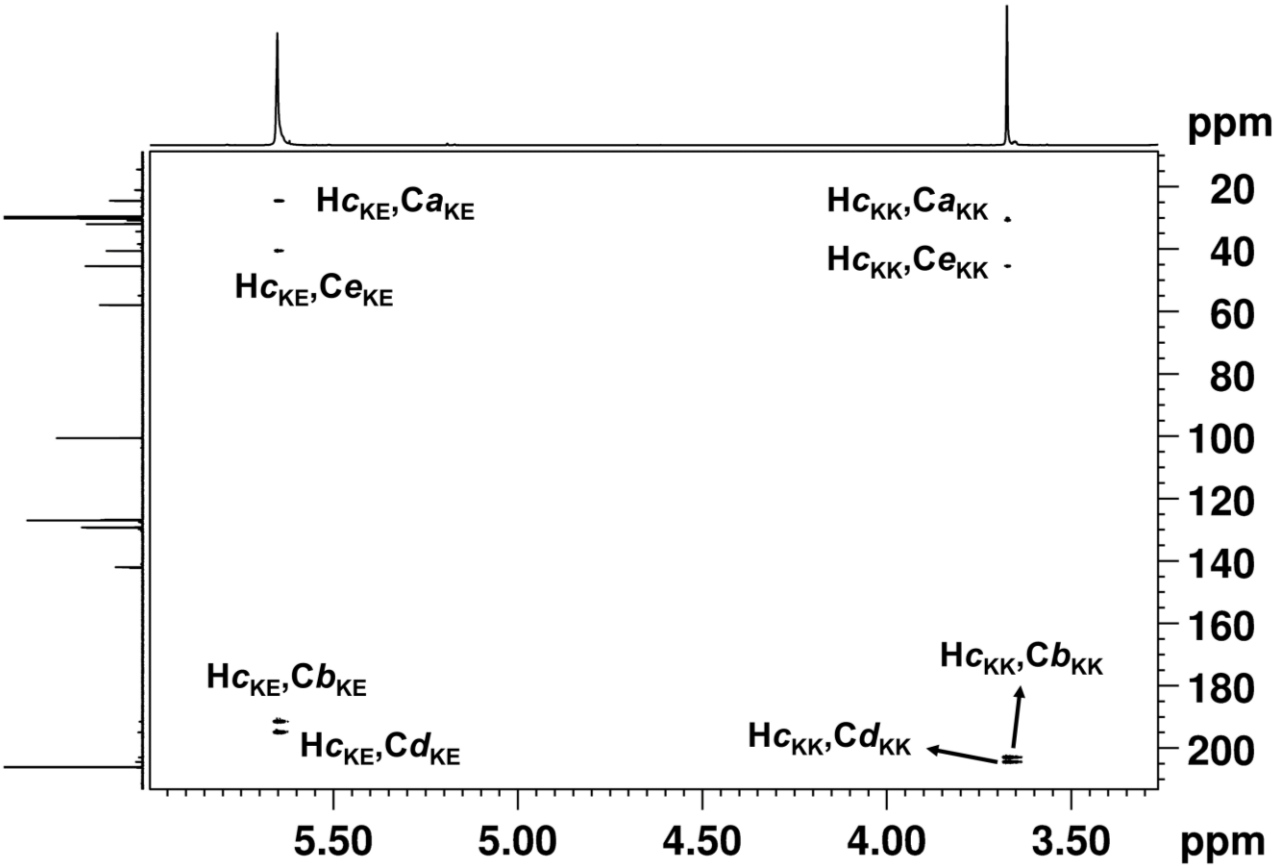

Figure S6. ^{1}H–^{13}C HMBC spectrum of H_2bdhb in acetone-d_6 for δ_H = 6.00–3.25 ppm and δ_C = 210–15 ppm (298 K, 600.13 MHz for F2, 150.90 MHz for F1). The labelling of the cross-peaks indicates the ^{1}H–^{13}C coupling (F2, F1). Processing parameters (TopSpin 4.3.0[1]) for F2 (x axis): SI = TD, LB = 1.00 Hz. Processing parameters for F1 (y axis): SI = 2·TD, LB = 0.30 Hz.

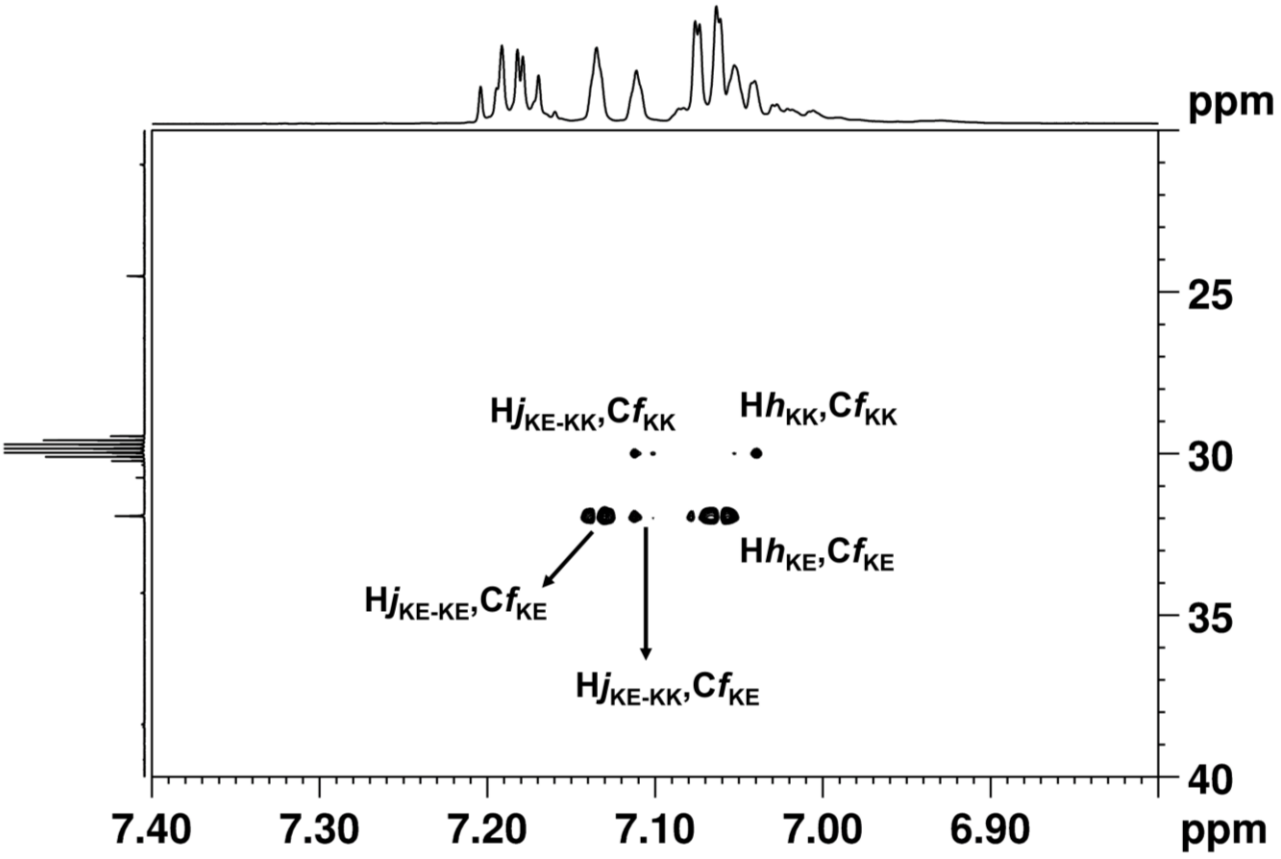

Figure S7. ^{1}H–^{13}C HMBC spectrum of H_2bdhb in acetone-d_6 for δ_H = 7.40–6.80 ppm and δ_C = 40–20 ppm (298 K, 600.13 MHz for F2, 150.90 MHz for F1). The labelling of the cross-peaks indicates the ^{1}H–^{13}C coupling (F2, F1). Processing parameters (TopSpin 4.3.0[1]) for F2 (x axis): SI = TD, LB = 1.00 Hz. Processing parameters for F1 (y axis): SI = 2·TD, LB = 0.30 Hz.

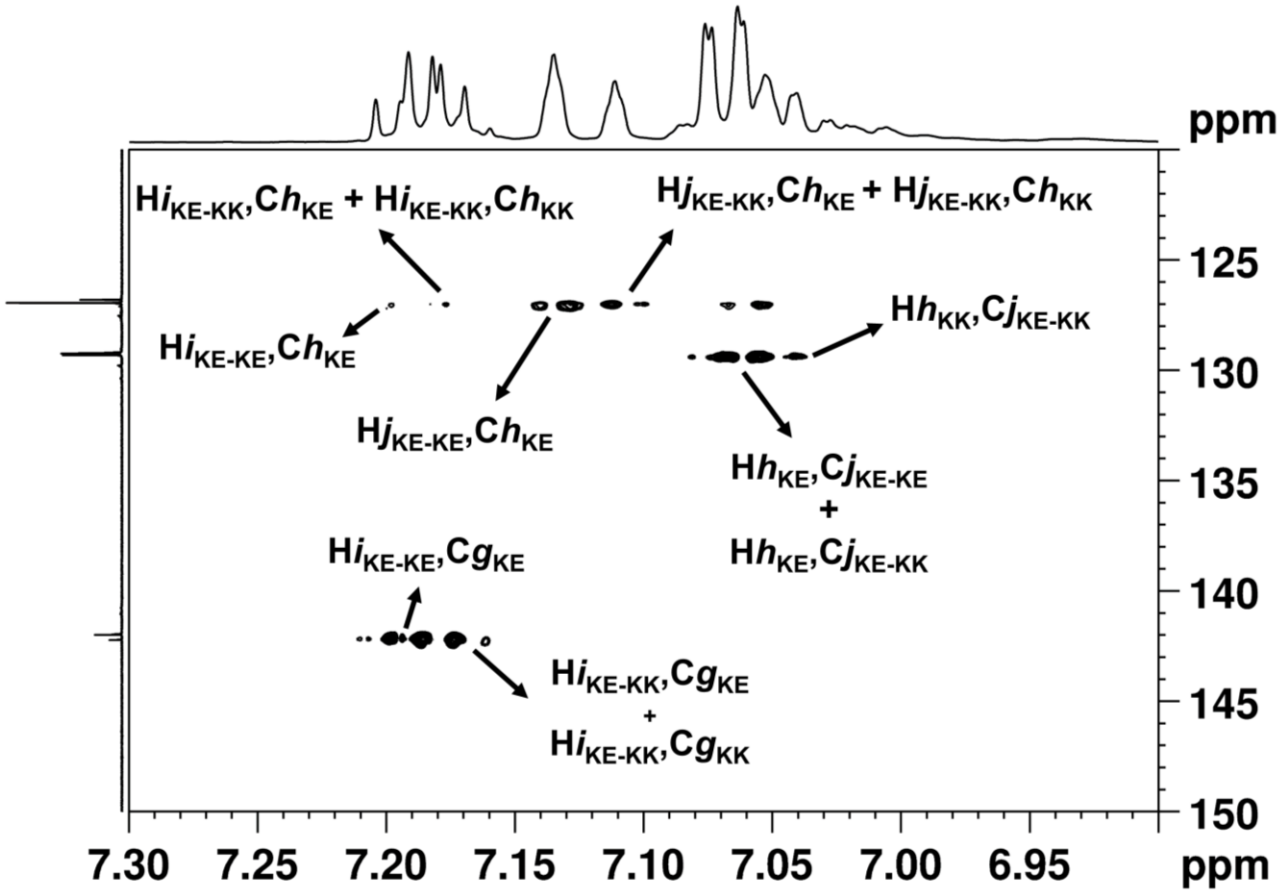

Figure S8. ^{1}H–^{13}C HMBC spectrum of H_2bdhb in acetone-d_6 for δ_H = 7.30–6.90 ppm and δ_C = 150–120 ppm (298 K, 600.13 MHz for F2, 150.90 MHz for F1). The labelling of the cross-peaks indicates the ^{1}H–^{13}C coupling (F2, F1). Processing parameters (TopSpin 4.3.0[1]) for F2 (x axis): SI = TD, LB = 1.00 Hz. Processing parameters for F1 (y axis): SI = 2·TD, LB = 0.30 Hz.

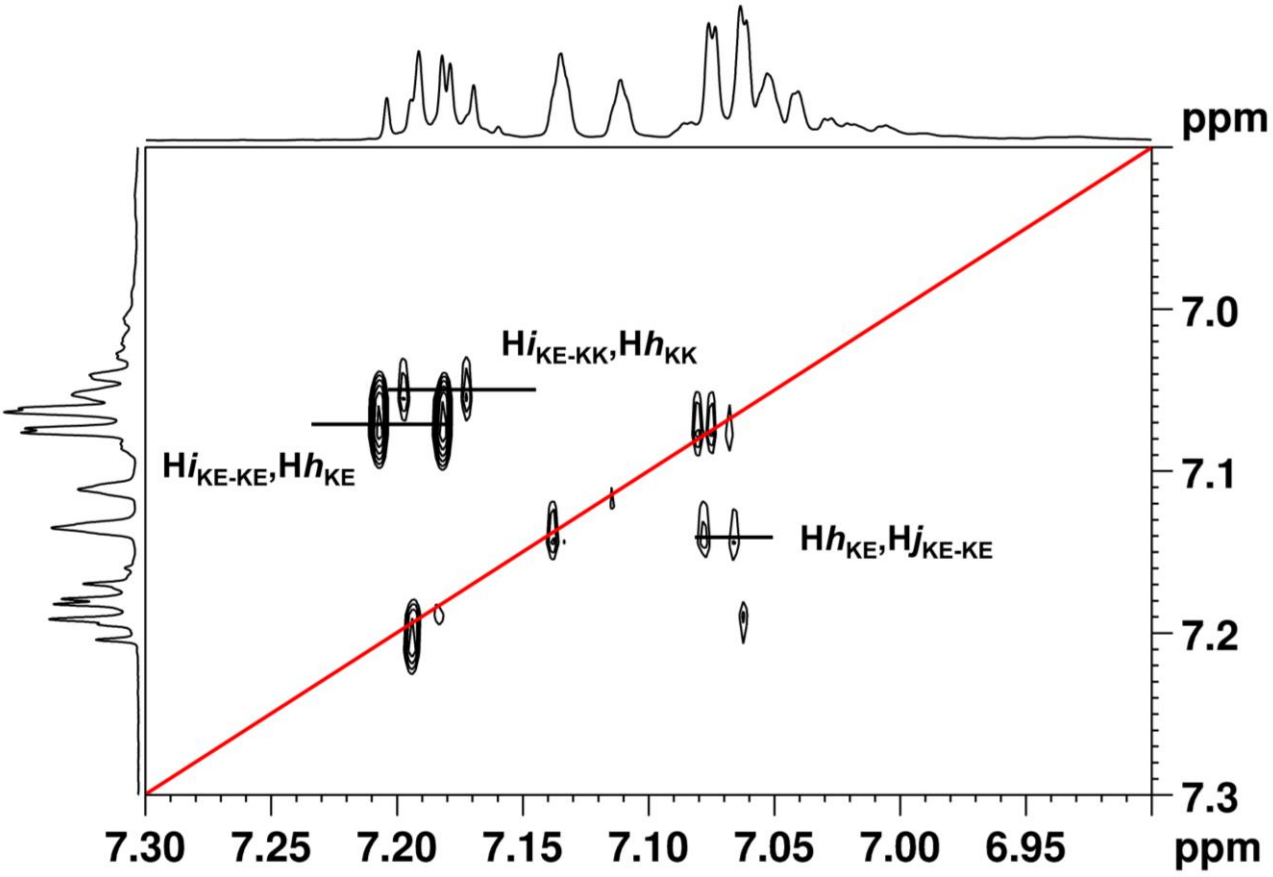

Figure S9. ^{1}H–^{1}H COSY spectrum of H_2bdhb in acetone-d_6 between 7.30 and 6.90 ppm (298 K, 600.13 MHz). The labelling of the cross-peaks indicates the ^{1}H–^{1}H coupling (F2, F1). The red line highlights the diagonal peaks. Processing parameters (TopSpin 4.3.0[1]) for F2 (x axis): SI = TD, LB = 0.10 Hz. Processing parameters for F1 (y axis): SI = 2·TD, LB = 0.30 Hz.

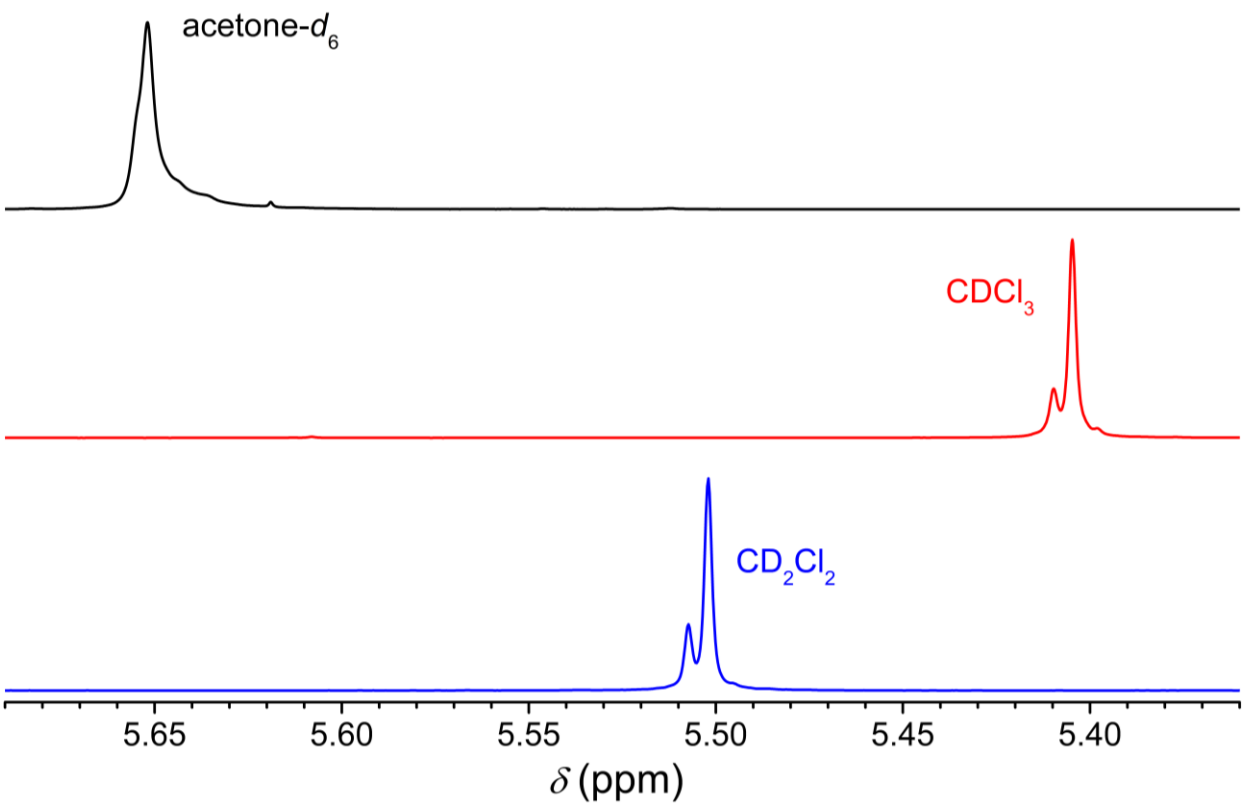

Figure S10. Comparison of the ^{1}H NMR spectra of H_2bdhb in the Hc_{KE} region in acetone-d_6 (black), $CDCl_3$ (red), and CD_2Cl_2 (blue).

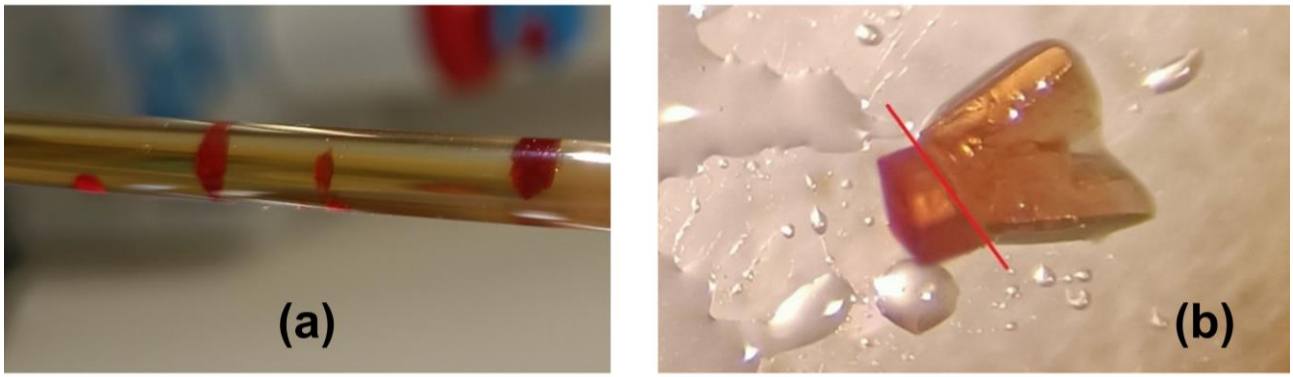

Figure S11. (a) Crystals of **2** obtained by liquid diffusion of *n*-hexane-py (90:10 v/v) into a solution of **1** in THF inside a 5-mm NMR tube. (b) Twinned individual whose left portion was cut with a razor blade along the red line and used for the single-crystal X-ray diffraction experiment.

Table S1. Crystal data and refinement parameters for **2**.

Chemical formula	$C_{56}H_{60}Co_2N_4O_8$
Formula weight	1034.94
T (K)	298(2)
Crystal size (mm^3)	0.22 × 0.21 × 0.14
Radiation	Mo-Kα (λ = 0.71073 Å)
Crystal system	triclinic
Space group	$P\bar{1}$
a (Å)	8.1332(3)
b (Å)	12.4868(5)
c (Å)	14.1570(5)
α (deg)	104.5937(13)
β (deg)	92.0834(12)
γ (deg)	107.1649(12)
V ($Å^3$)	1319.83(9)
Z	1
ρ_{calcd} (g cm^{-3})	1.302
$2\theta_{min}/2\theta_{max}$ (deg)	3.550/53.108
Reflections collected/independent	17602/5441
R_{int}	0.0279
No. of parameters/restraints	318/0
$R1/wR2$ (all data)	0.0355/0.0791
$R1/wR2$ ($I \geq 2\sigma(I)$)	0.0284/0.0743
GOF	1.026
Largest diff. peak/hole ($eÅ^{-3}$)	0.240/−0.153

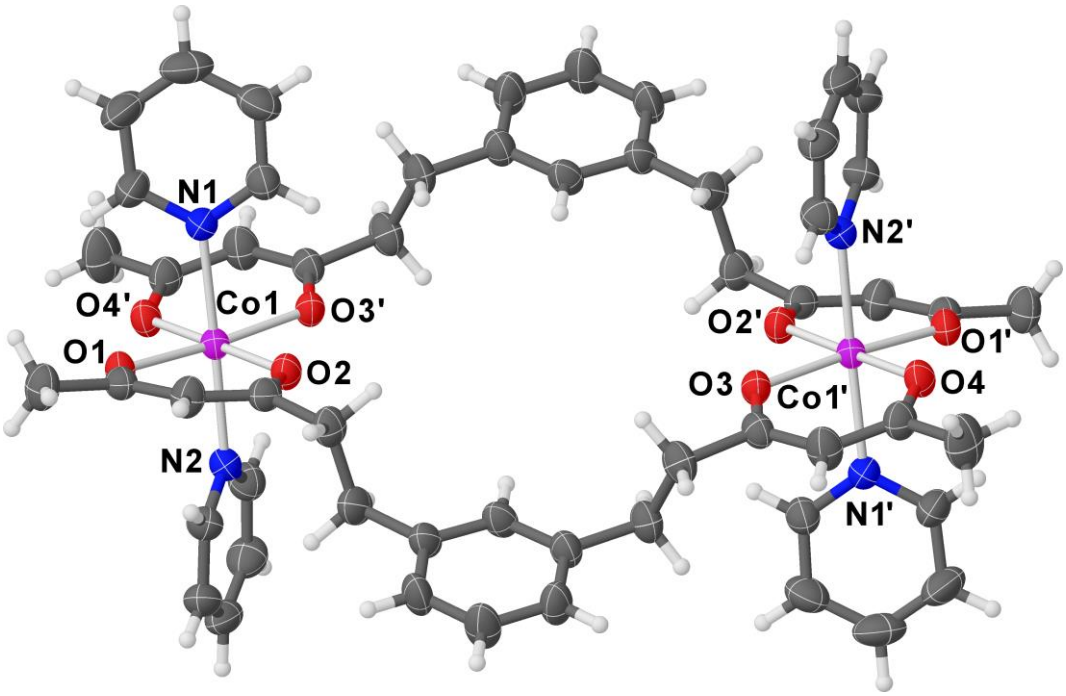

Figure S12. Molecular structure of **2** with the atom labelling scheme (Color code: C = dark gray, H = white, O = red, N = blue, Co = magenta) and displacement ellipsoids drawn at the 40% probability level. Primed atoms are related to unprimed ones by inversion through the center of the molecule. The rotational disorder of methyl groups is omitted.

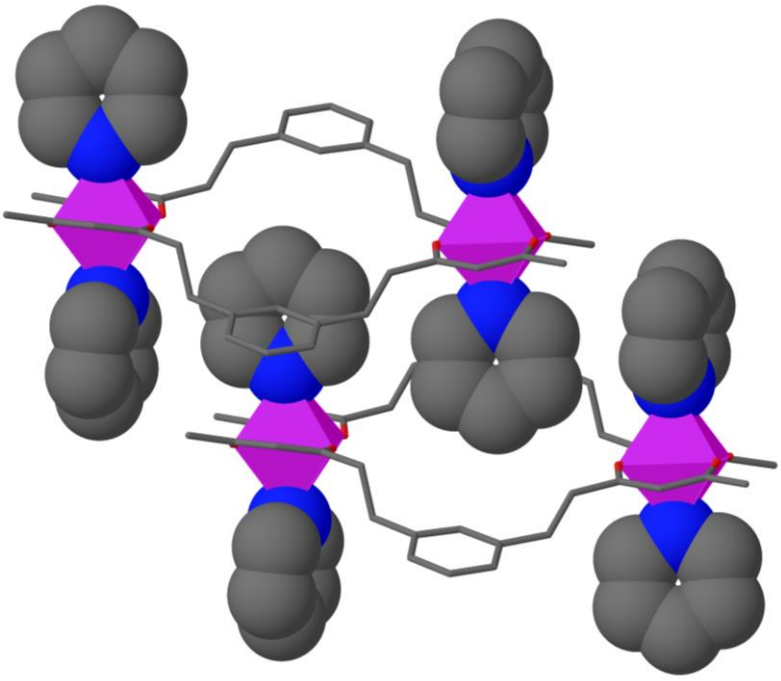

Figure S13. Crystal packing in **2**, showing the position of the py rings relative to the central molecular pores. The coordination environments of the cobalt(II) ions are shown as magenta *polyhedra*, the py rings are drawn using a *space-filling* model (Color code: C = black, N = blue), and the organic skeleton of the $bdhb^{2-}$ ligands is depicted with grey capped sticks. H atoms are omitted for clarity.

Table S2. Bond-valence sum (BVS) calculations on **2**.[a]

Atom	BVS with Co^{+2} parameters	BVS with Co^{+3} parameters
Co1	2.102	1.847

[a]Bond-valence sum parameters (R_0; B) were taken from file bvparm2020.cif available at https://www.iucr.org/resources/data/datasets/bond-valence-parameters: Co^{+2}–N^{-3} (1.72; 0.37), Co^{+2}–O^{-2} (1.692; 0.37), Co^{+3}–N^{-3} (1.69; 0.37), Co^{+3}–O^{-2} (1.637; 0.37).

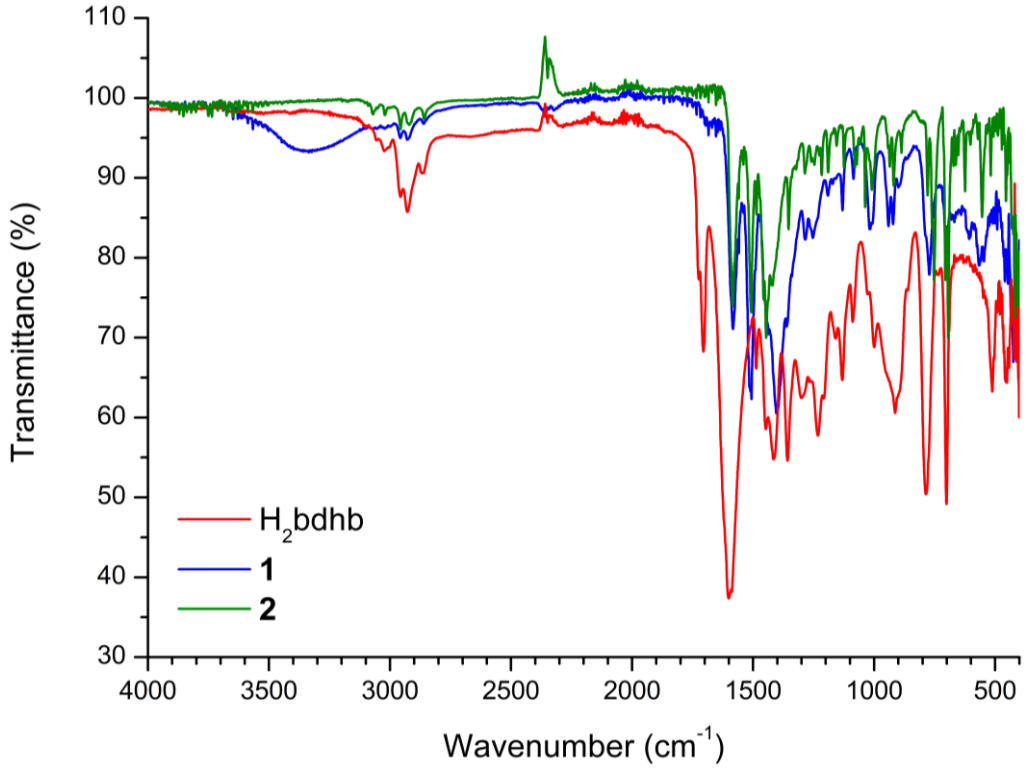

Figure S14. FT-IR spectra of H_2bdhb (red), **1** (blue), and **2** (green).

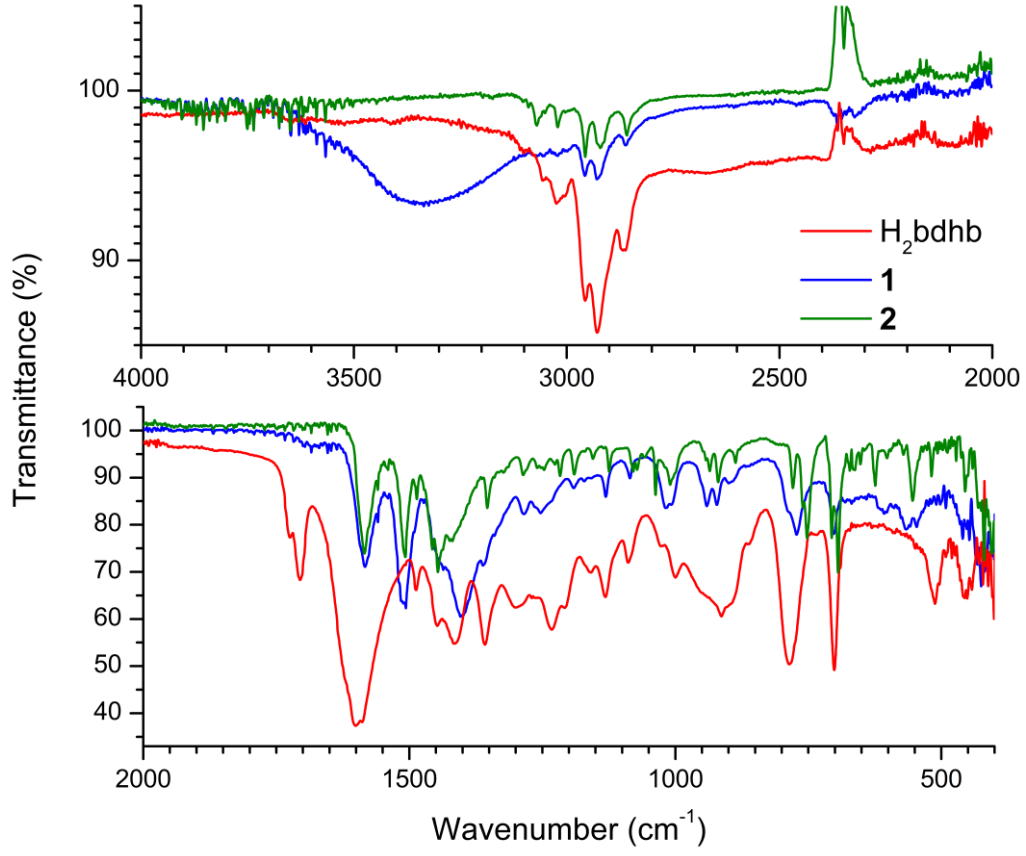

Figure S15. FT-IR spectra of H_2bdhb (red), **1** (blue), and **2** (green), zoomed in the region 4000-2000 cm^{-1} (top) and 2000-400 cm^{-1} (bottom).

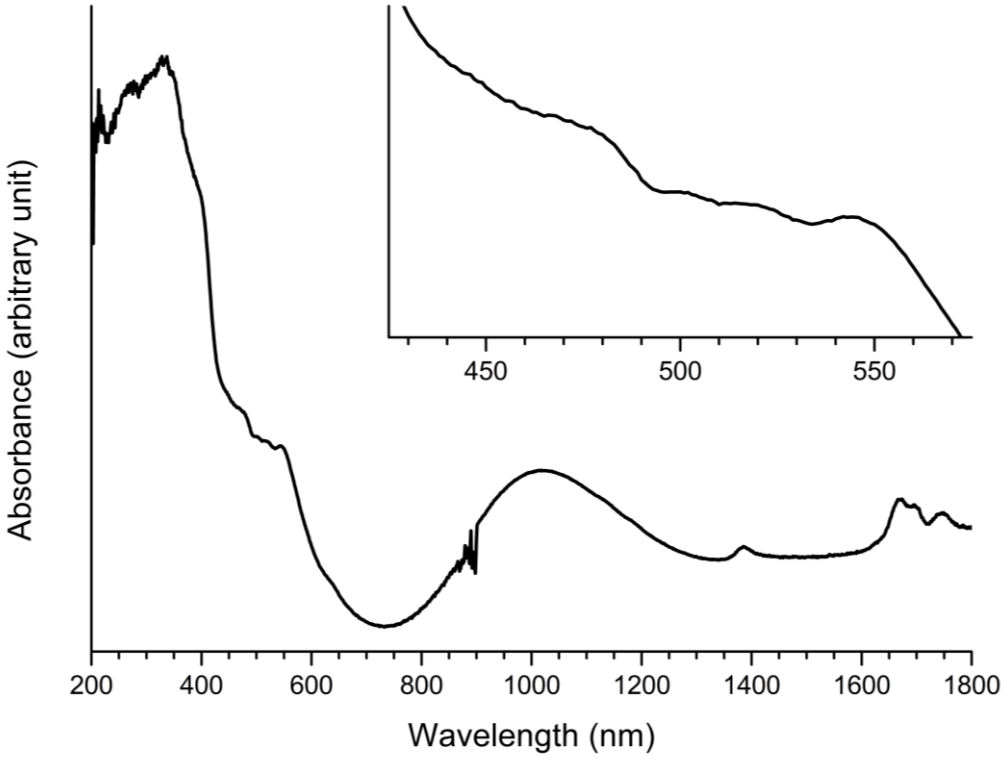

Figure S16. UV-Vis-NIR reflectance spectrum of **2**.

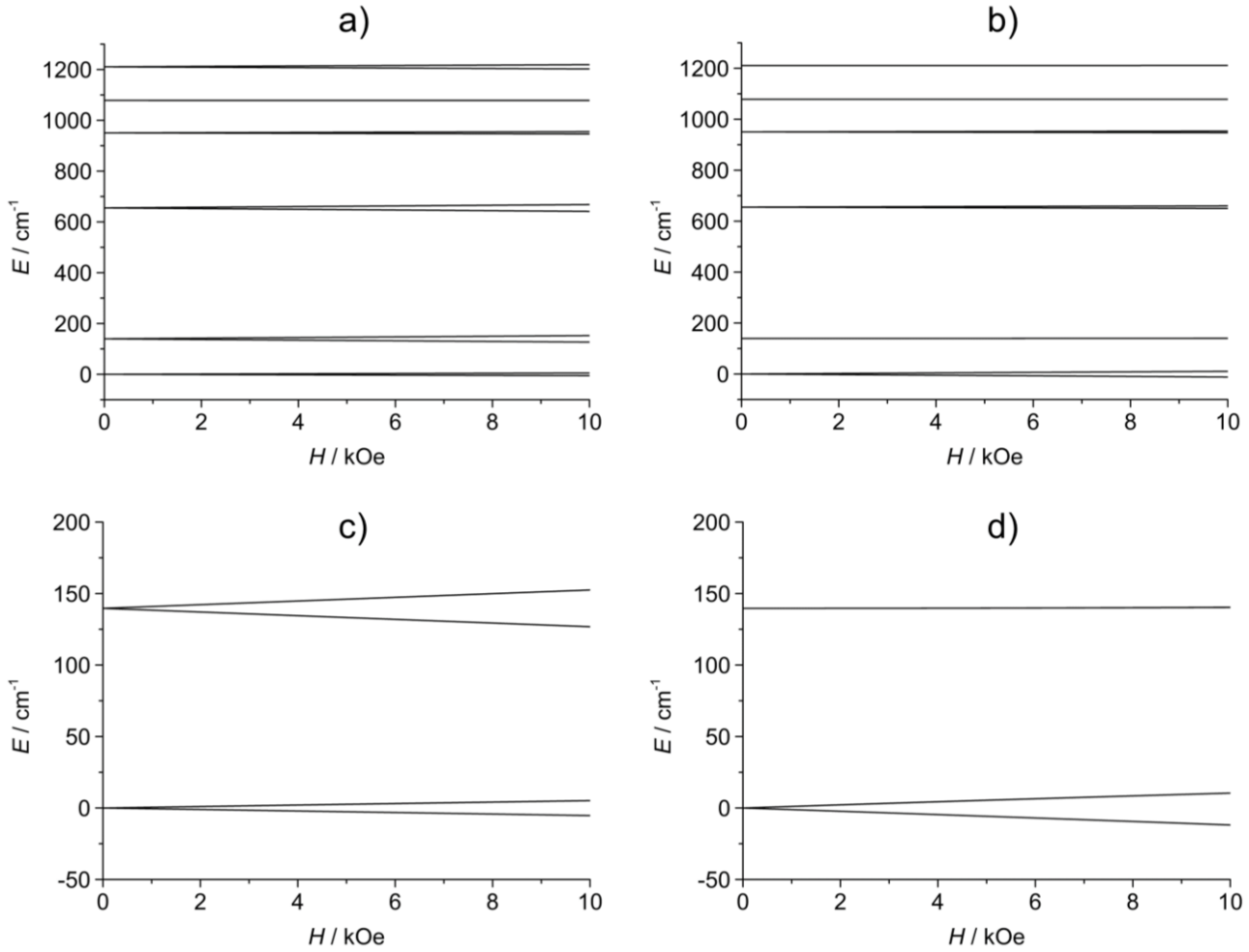

Figure S17. Zeeman diagram of the twelve electronic levels arising from Eq. (1), calculated with $A\kappa = -1.2$, $B_2^0 = 159.5$ cm^{-1}, and the magnetic field applied along z (a) or orthogonal to z (b). Panels (c) and (d) display the zoom of the lowest-lying electronic levels in (a) and (b), respectively.

Supplementary Note 2: AC magnetic susceptibility data fitting. AC susceptibility curves as a function of frequency (v) were fitted with a generalized Debye model[2,3] by using a homemade script in MATLAB.[4] The software applies the analytical model to fit χ'_M and χ''_M components simultaneously, yielding three best-fit parameters as output, i.e. $\chi_T - \chi_S$ = isothermal susceptibility – adiabatic susceptibility, α = distribution linewidth, and τ = relaxation time of the magnetization. Plots of χ'_M vs. v and χ''_M vs. v collected at different values of T and H_{DC} are reported together with best-fit curves in Figures S18-S20. The list of best-fit parameters for each dataset is reported in Tables S3-S5. Plots of $\chi_T - \chi_S$ and α as functions of T and H_{DC} are presented in Figures S21-S23.

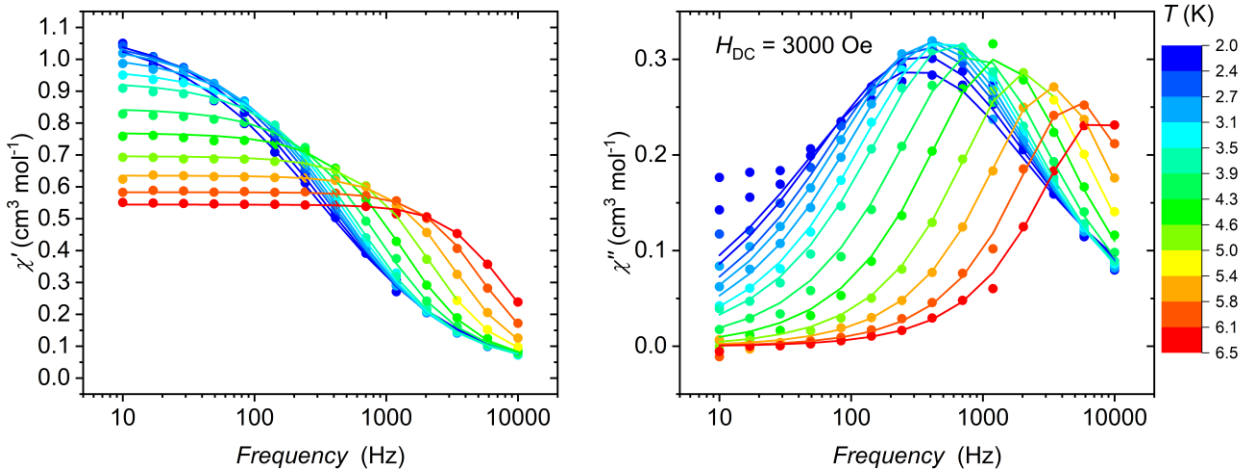

Figure S18. Experimental χ'_M (left) and χ''_M (right) curves as a function of frequency for **2**, collected at H_{DC} = 3 kOe and different temperatures between 2 and 6.5 K. The solid lines provide the best fit using the generalized Debye model.

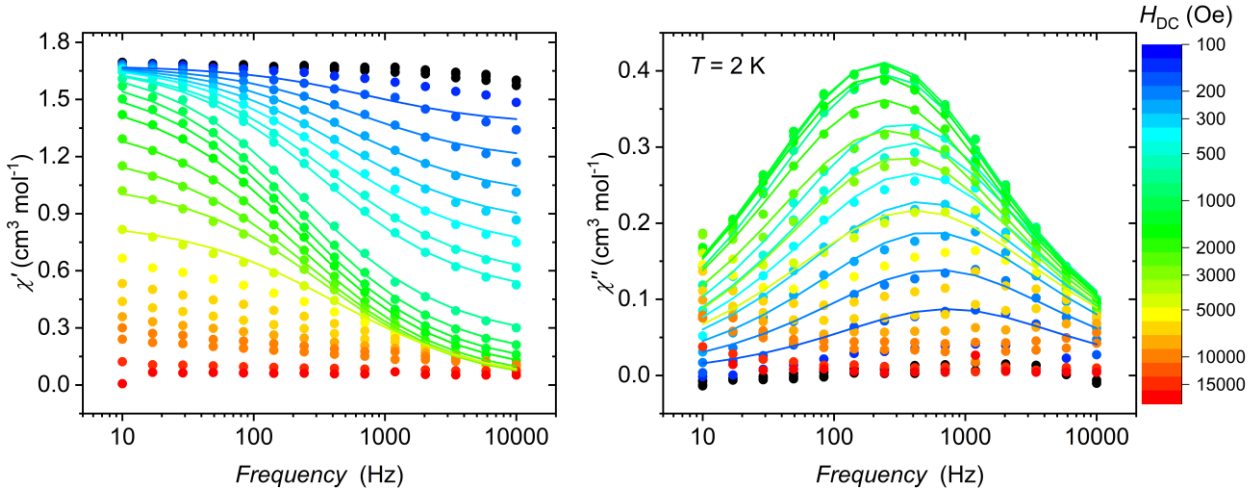

Figure S19. Experimental χ'_M (left) and χ''_M (right) curves as a function of frequency for **2**, collected at T = 2 K and H_{DC} values up to 20 kOe. The solid lines provide the best fit using the generalized Debye model.

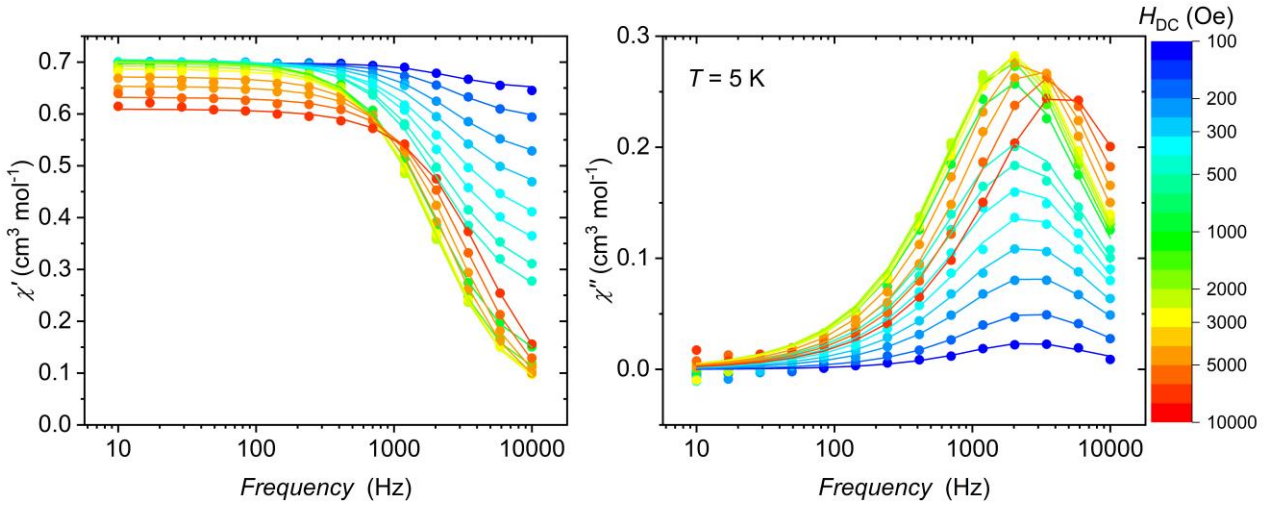

Figure S20. Experimental χ'_{M} (left) and χ''_{M} (right) curves as a function of frequency for **2**, collected at T = 5 K and H_{DC} values up to 10 kOe. The solid lines provide the best fit using the generalized Debye model.

Table S3. Best-fit parameters for the χ'_{M} and χ''_{M} data in Figure S18.

T (K)	$\chi_T - \chi_S$ (cm^3 mol^{-1})	$\sigma(\chi_T - \chi_S)$ (cm^3 mol^{-1})	τ (10^{-4} s)	$\sigma(\tau)$ (10^{-4} s)	α	$\sigma(\alpha)$
2.01	1.10	0.33	5.10	1.16	0.39	0.11
2.26	1.10	0.23	4.73	0.74	0.35	0.08
2.51	1.06	0.12	4.24	0.33	0.32	0.04
2.76	1.03	0.09	3.92	0.24	0.30	0.03
3.01	0.99	0.04	3.50	0.08	0.27	0.01
3.26	0.94	0.07	3.03	0.14	0.24	0.03
3.51	0.90	0.06	2.62	0.10	0.22	0.03
4.00	0.80	0.15	1.87	0.17	0.17	0.07
4.50	0.73	0.15	1.21	0.08	0.12	0.08
5.00	0.65	0.10	0.76	0.03	0.08	0.06
5.50	0.59	0.04	0.48	0.01	0.05	0.03
6.00	0.53	0.07	0.31	0.02	0.02	--
6.50	0.49	0.06	0.21	0.02	0.02	--

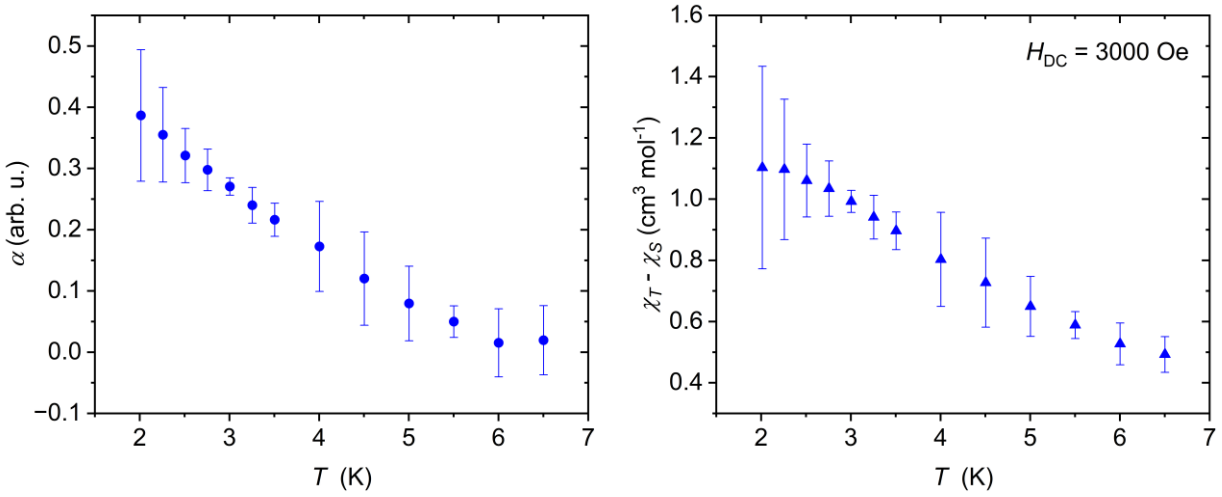

Figure S21. Plot of the best-fit $\chi_{\mathrm{T}} - \chi_{\mathrm{S}}$ and α parameters as a function of T at H_{DC} = 3 kOe for **2** (Table S3).

Table S4. Best-fit parameters for the χ'_{M} and χ''_{M} data in Figure S19.

H_{DC} (Oe)	$\chi_T - \chi_S$ ($\mathrm{cm^3\ mol^{-1}}$)	$\sigma(\chi_T - \chi_S)$ ($\mathrm{cm^3\ mol^{-1}}$)	τ (10^{-4} s)	$\sigma(\tau)$ (10^{-4} s)	α	$\sigma(\alpha)$
175	0.30	--	2.16	1.76	0.36	0.32
225	0.52	0.38	2.60	1.47	0.38	0.21
275	0.71	0.39	2.92	1.22	0.38	0.16
325	0.87	0.33	3.37	1.03	0.39	0.11
375	1.02	0.35	3.95	1.06	0.39	0.11
435	1.15	0.34	4.20	0.90	0.38	0.10
500	1.25	0.25	4.72	0.70	0.38	0.07
750	1.49	0.17	6.35	0.56	0.38	0.04
1000	1.54	0.16	6.86	0.55	0.38	0.04
1250	1.54	0.16	7.15	0.54	0.38	0.04
1500	1.50	0.14	7.20	0.54	0.38	0.04
2000	1.39	0.22	6.71	0.84	0.39	0.06
2500	1.24	0.29	6.03	1.12	0.39	0.08
3000	1.07	0.34	4.78	1.05	0.38	0.11
4000	0.87	0.50	3.78	1.68	0.41	0.18

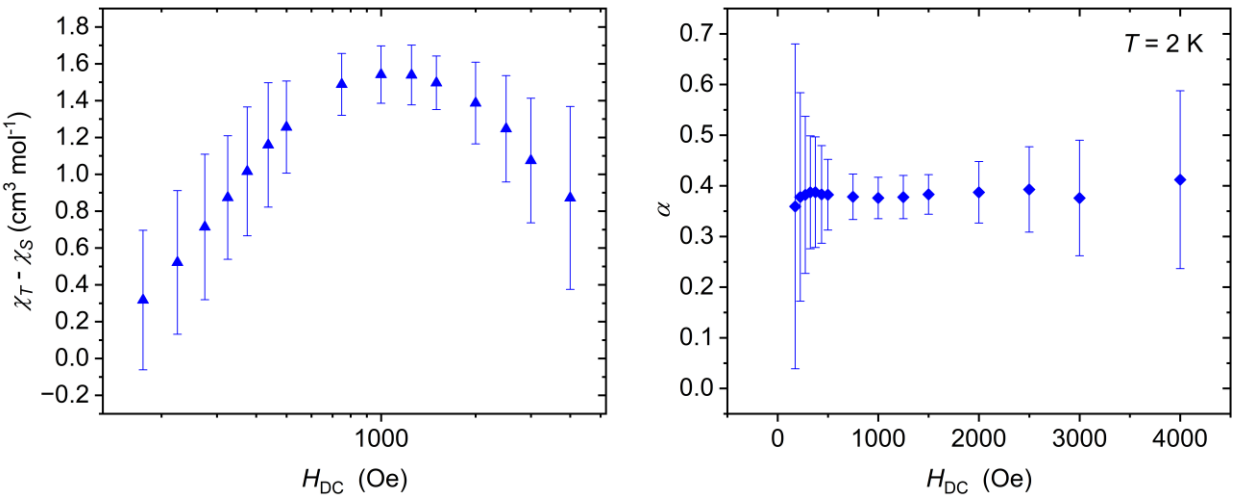

Figure S22. Plot of the best-fit $\chi_{\mathrm{T}} - \chi_{\mathrm{S}}$ and α parameters as a function of H_{DC} at T = 2 K for **2** (Table S4).

Table S5. Best-fit parameters for the χ'_{M} and χ''_{M} data in Figure S20.

H_{DC} (Oe)	$\chi_T - \chi_S$ ($\mathrm{cm^3\ mol^{-1}}$)	$\sigma(\chi_T - \chi_S)$ ($\mathrm{cm^3\ mol^{-1}}$)	τ (10^{-4} s)	$\sigma(\tau)$ (10^{-4} s)	α	$\sigma(\alpha)$
125	0.05	0.02	0.63	0.12	0.05	--
175	0.11	0.03	0.58	0.07	0.05	--
225	0.19	0.04	0.60	0.05	0.1	--
275	0.25	0.04	0.62	0.03	0.09	0.05
325	0.32	0.06	0.64	0.05	0.10	0.07
375	0.37	0.08	0.69	0.05	0.09	0.08
435	0.43	0.08	0.72	0.05	0.10	0.07
500	0.47	0.09	0.74	0.05	0.09	0.07
1000	0.59	0.12	0.82	0.05	0.09	0.07
1500	0.63	0.11	0.84	0.05	0.08	0.07
2000	0.65	0.10	0.83	0.04	0.09	0.06
2500	0.64	0.09	0.80	0.04	0.08	0.05
3000	0.64	0.08	0.76	0.03	0.08	0.04
4000	0.63	0.05	0.66	0.01	0.08	0.03
5000	0.62	0.04	0.56	0.01	0.08	0.02
6000	0.60	0.05	0.46	0.01	0.09	0.03
7000	0.59	0.05	0.36	0.01	0.11	0.03

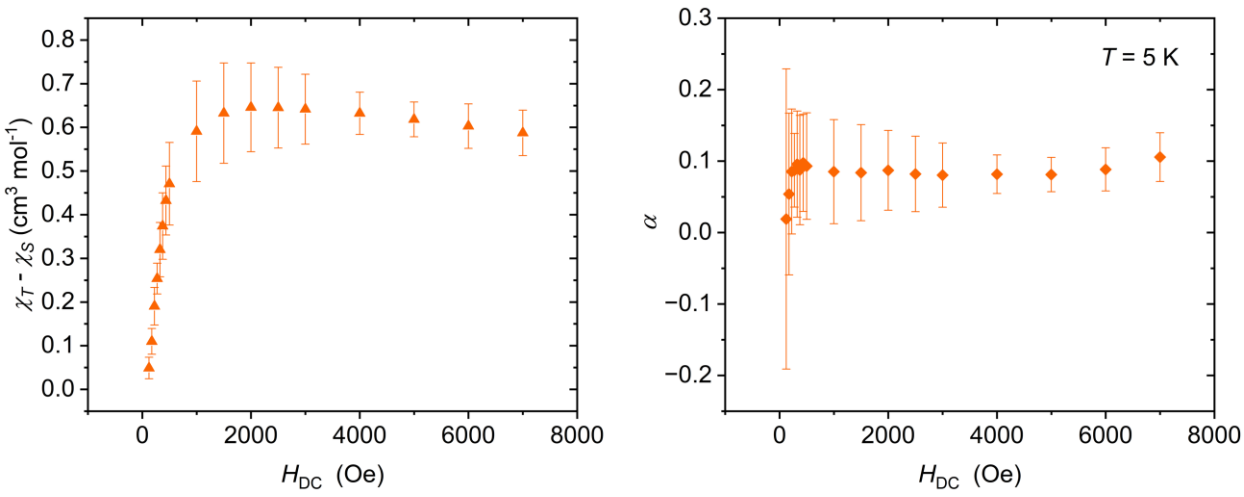

Figure S23. Plot of the best-fit $\chi_{\mathrm{T}} - \chi_{\mathrm{S}}$ and α parameters as a function of H_{DC} at T = 5 K for **2** (Table S5).

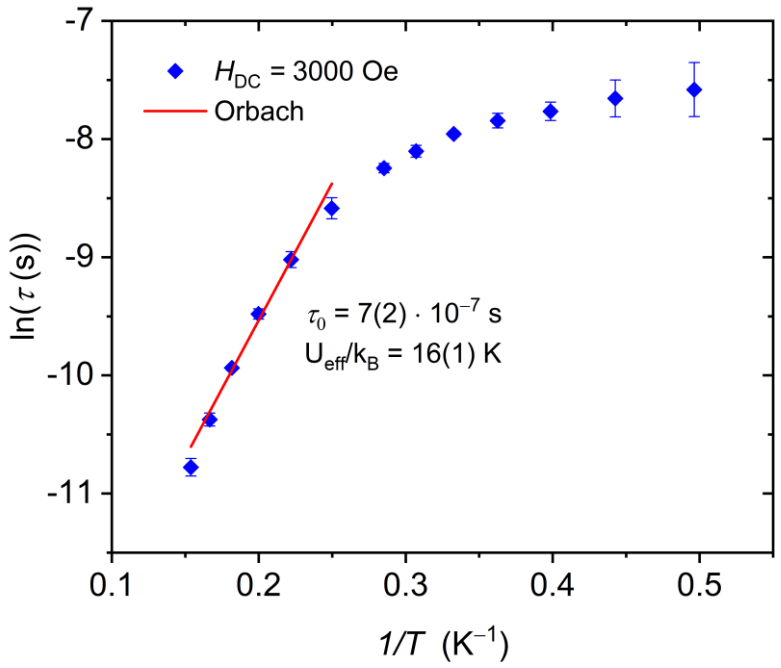

Figure S24. τ vs. T data for **2** at H_{DC} = 3 kOe (solid blue diamonds) and linear fit of the high-temperature portion using Arrhenius law, i.e. $\tau = \tau_0 \exp(U_{eff}/k_B T)$, to describe Orbach relaxation (red line).

Supplementary Note 3: Fitting of the CW-EPR spectra of 2 (powder). The CW-EPR spectrum of the powder sample of **2** was initially simulated by manually varying the parameters reported in Table S6 until the best visual agreement between simulation and experimental results was achieved. The best-simulation parameter set was then used as an initial guess for the fitting protocol exploited to get a more reliable estimation of hyperfine and anisotropic strain tensor components. To do so, we used a hybrid fitting protocol based on the least-square fitting suite provided by EasySpin.[5] The first process involved a genetic fitting algorithm, while the second stemmed from a Nelder/Mead simplex algorithm. While the first is best suited for targeting a global minimum of the fitting outcome, using a wide variety of parameter combinations, the second algorithm is best suited for searching for a local minimum. Given the large number of parameters, their correlation, and the poor spectral resolution, we found that the genetic algorithm required significant time to reach the global minimum. For this reason, the first algorithm was run for ca. 300 generations to guarantee a statistically considerable number of combinations and a reliable estimation of the best-fit parameter set. Then, this set was used as an initial guess for the Nelder/Mead simplex algorithm, reducing the variation range of the initial parameter set. In this way, a faster and more accurate estimation of parameter values and their uncertainties was successfully achieved. The best-fit parameter set obtained using this protocol is reported in Table 4 of the main text, while the computed spectrum is reported in Figure 6a.

Table S6. Manual-simulation EPR parameters for the powder sample of **2** at T = 10 K.[a]

S'	1/2
g'_x	5.75
g'_y	4.55
g'_z	2.00
A'_x (MHz)	0
A'_y (MHz)	0
A'_z (MHz)	400
Γ_x [b] (MHz)	2700
Γ_y [b] (MHz)	1800
Γ_z [b] (MHz)	520

[a]Based on the effective SH in Eq. (6) of the main text. [b]Components of anisotropic residual linewidth vector $\mathbf{\Gamma} = [\Gamma_x\ \Gamma_y\ \Gamma_z]$ for modeling linewidths; isotropic broadening was modeled with a pseudo-Voigtian line-shape of 2 mT for both Gaussian and Lorentzian contributions.

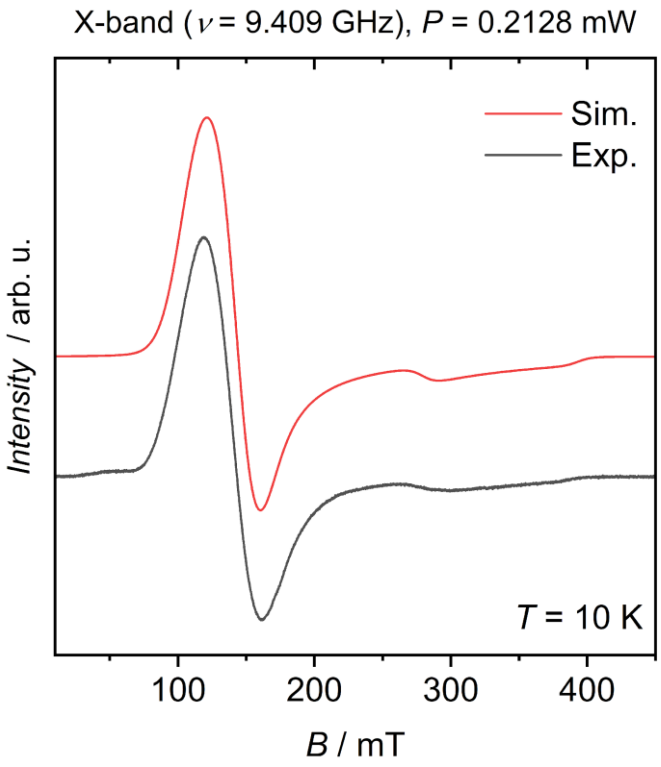

Figure S25. Experimental EPR spectrum of **2** (powder) at 10 K together with its simulation using the parameter set in Table S6.

Table S7. NEVPT2 calculated energies of the first six Kramers doublets (KDs) for **2**.

KD	Energy (cm^{-1})
1	0
2	188.5
3	778.3
4	1125.4
5	1274.9
6	1393.8

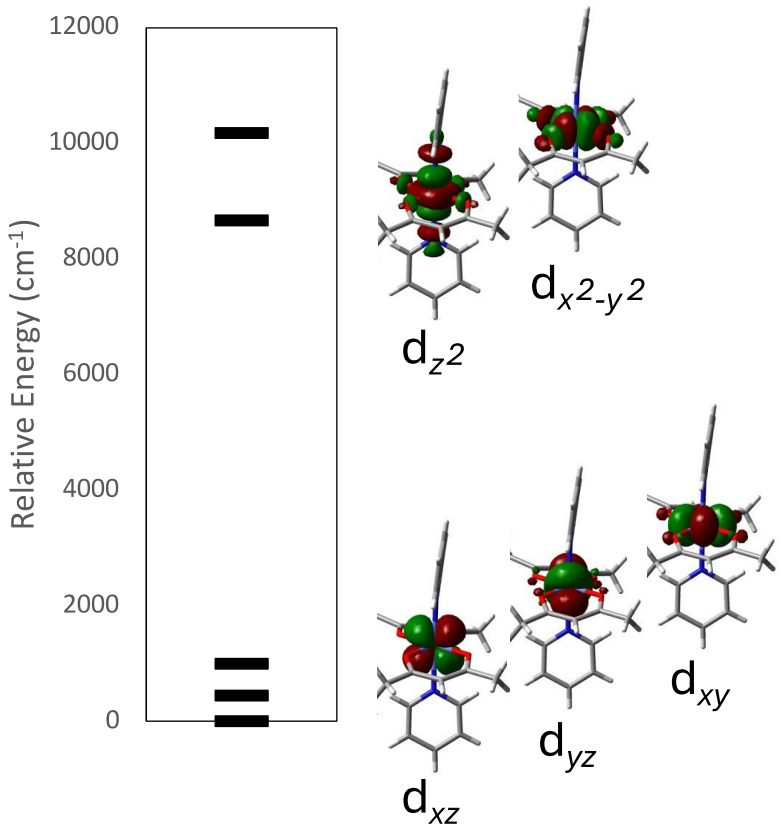

Figure S26. Energy splitting and corresponding orbitals obtained from AILFT calculations. Orbitals are drawn following their energy ordering. For simplicity, only the close coordination environment of **2** is shown in stick representation. Cobalt, oxygen, nitrogen, carbon and hydrogen are represented in light blue, red, blue, grey, and white, respectively.

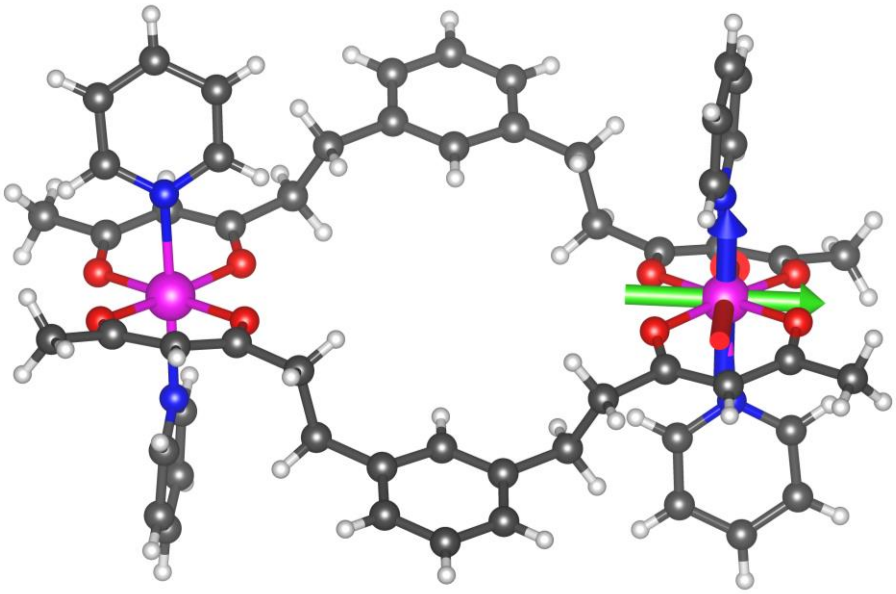

Figure S27. Ball-and-stick drawing of complex **2** including the principal directions of the **g'** tensor as colored arrows. Red, green, and blue arrows indicate the direction of the g'_x, g'_y, and g'_z components, respectively.

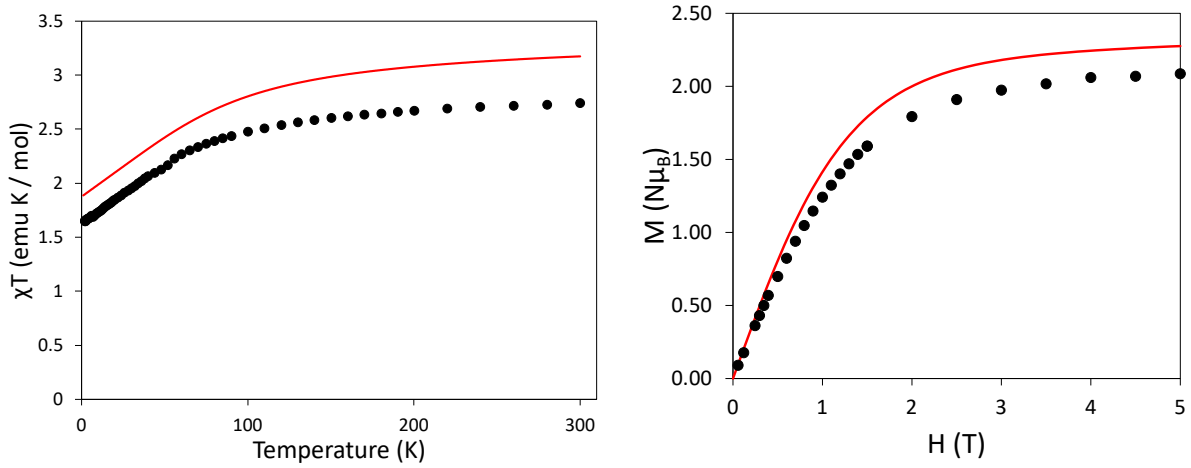

Figure S28. Experimental (black dots) and calculated (red lines) susceptibility curves (left) and magnetization data at 2 K (right) for **2**.

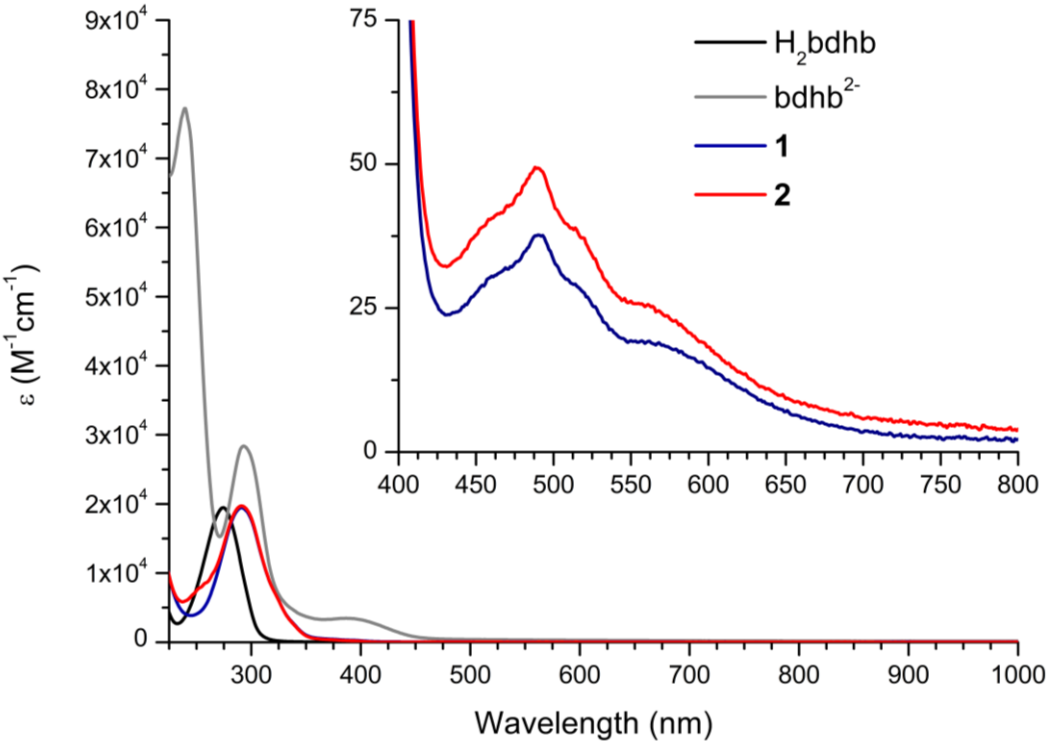

Figure S29. UV-Vis-NIR spectra of H_2bdhb (black), bdhb^{2-} (gray), **1** (navy), and **2** (red) in THF (bdhb^{2-} was obtained by adding excess *t*-BuOK to H_2bdhb). The inset shows the region between 400 and 800 nm, which contains the crystal-field bands of high-spin cobalt(II) ion.

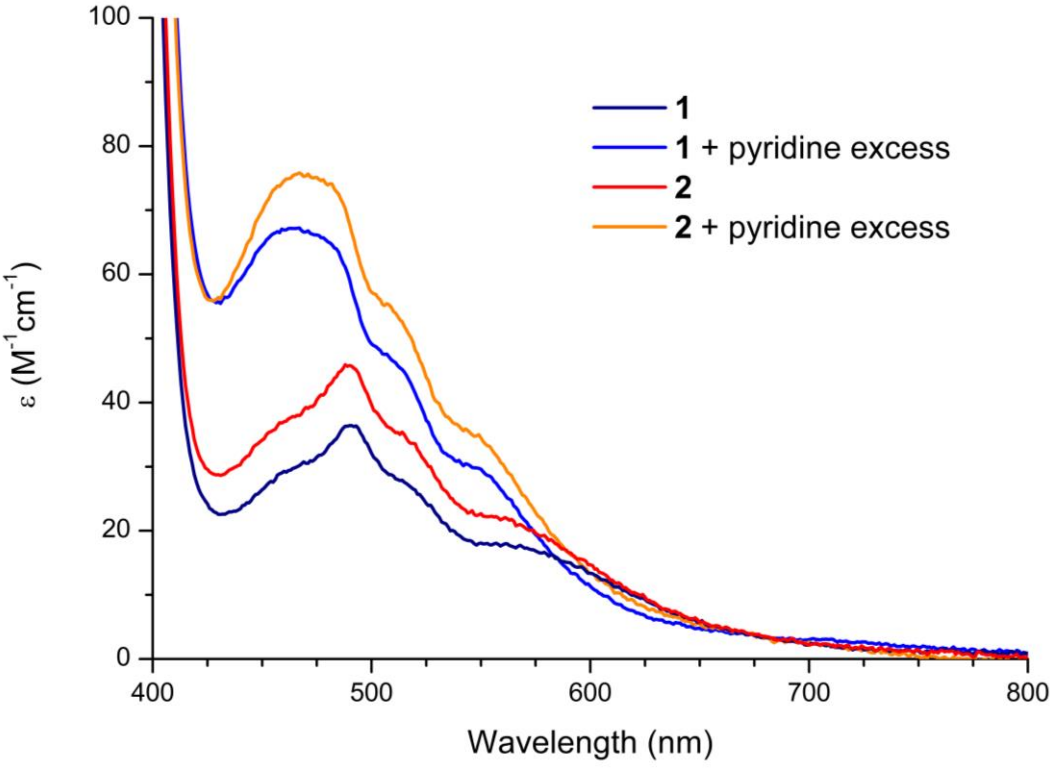

Figure S30. UV-Vis spectra of **1** (navy/blue) and **2** (red/orange) in THF, before/after the addition of an excess of pyridine.

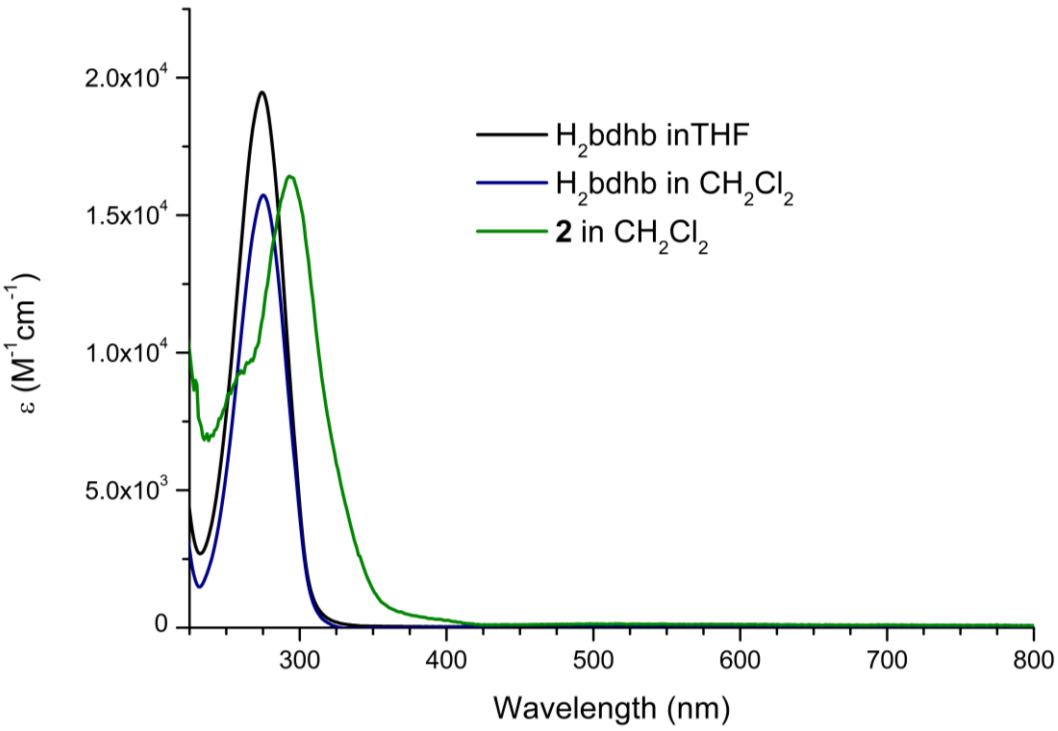

Figure S31. UV-Vis spectra of H_2bdhb in THF (black), H_2bdhb in CH_2Cl_2 (blue), and **2** in CH_2Cl_2 (olive).

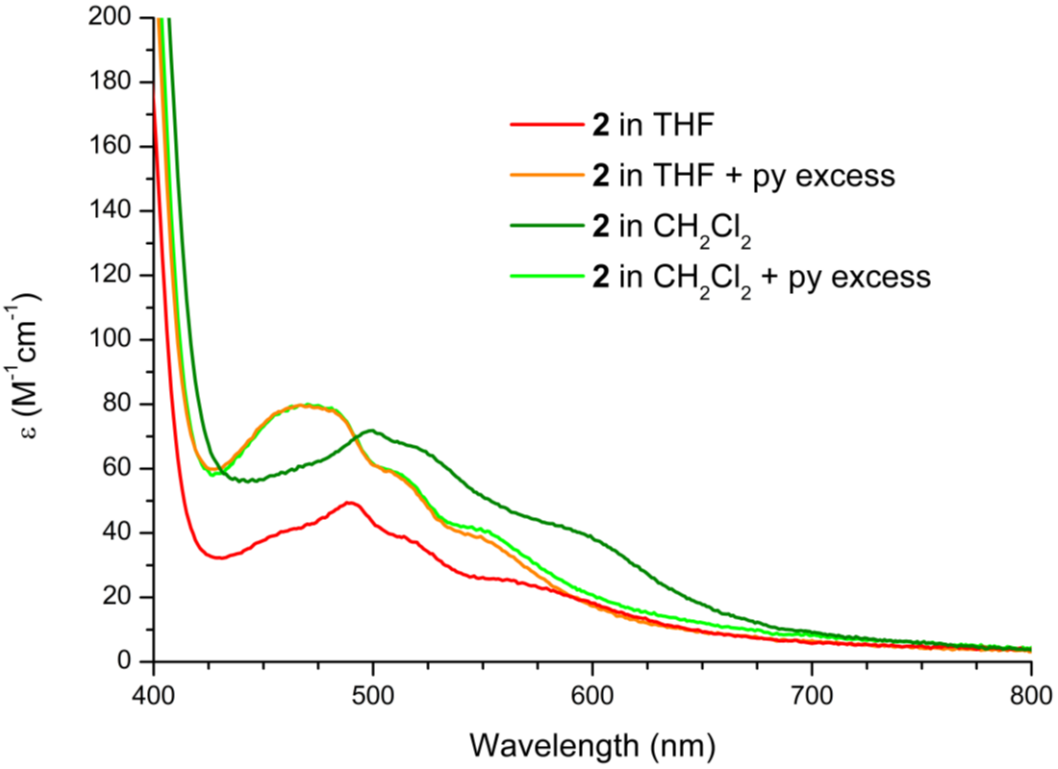

Figure S32. UV-Vis spectrum of **2** in THF (red/orange) and in CH_2Cl_2 (olive/green), before/after the addition of an excess of pyridine.

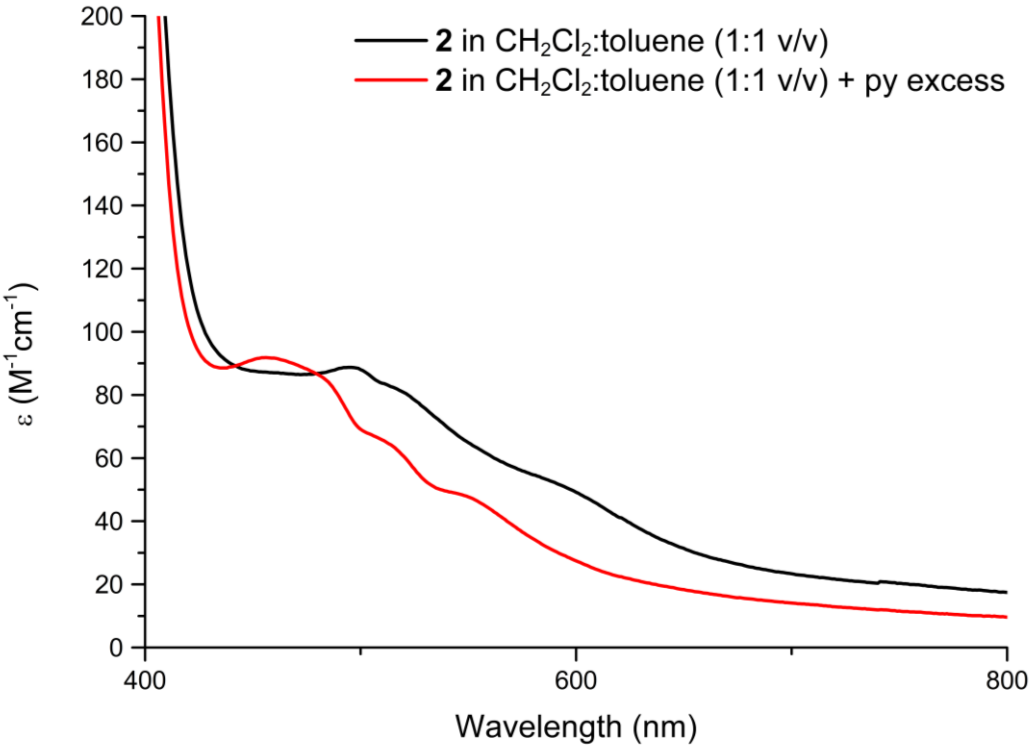

Figure S33. UV-Vis spectrum of **2** in CH_2Cl_2/toluene (1:1 v/v) before (black) and after (red) the addition of an excess of pyridine.

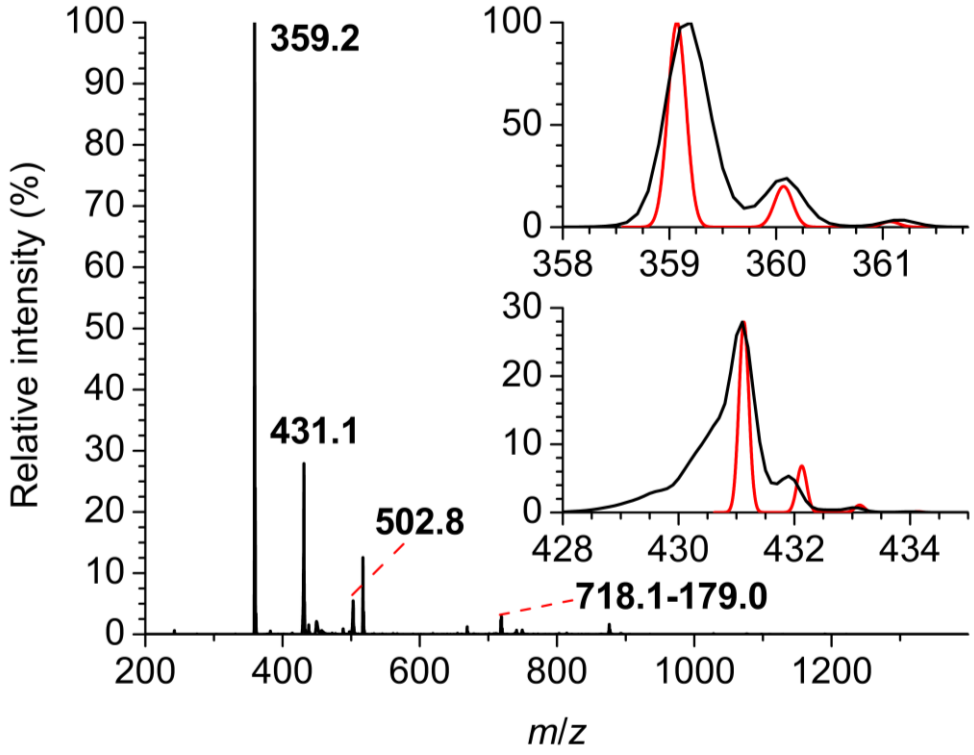

Figure S34. ESI-MS spectrum of **1** (direct infusion, THF, positive-ion mode). The insets show the experimental (black line) and simulated (red line) isotopic patterns of the peaks at *m*/*z* = 359.2 and 431.1, attributed to $[Co(bdhb)]^+$ and $([Co(bdhb)(THF)]^+$, respectively.

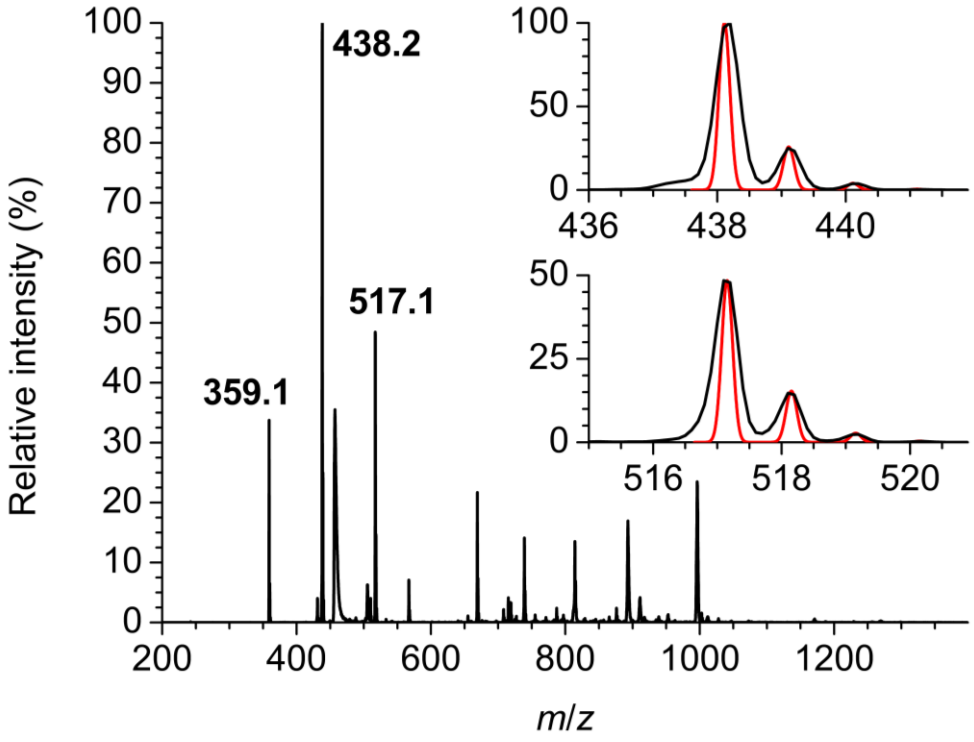

Figure S35. ESI-MS spectrum of **2** (direct infusion, THF, positive ion mode). The inset shows the experimental (black line) and simulated (red line) isotopic patterns of the peaks at *m*/*z* = 438.2 and 517.1, attributed to $[Co(bdhb)(py)]^+$ and $[Co(bdhb)(py)_2]^+$, respectively.

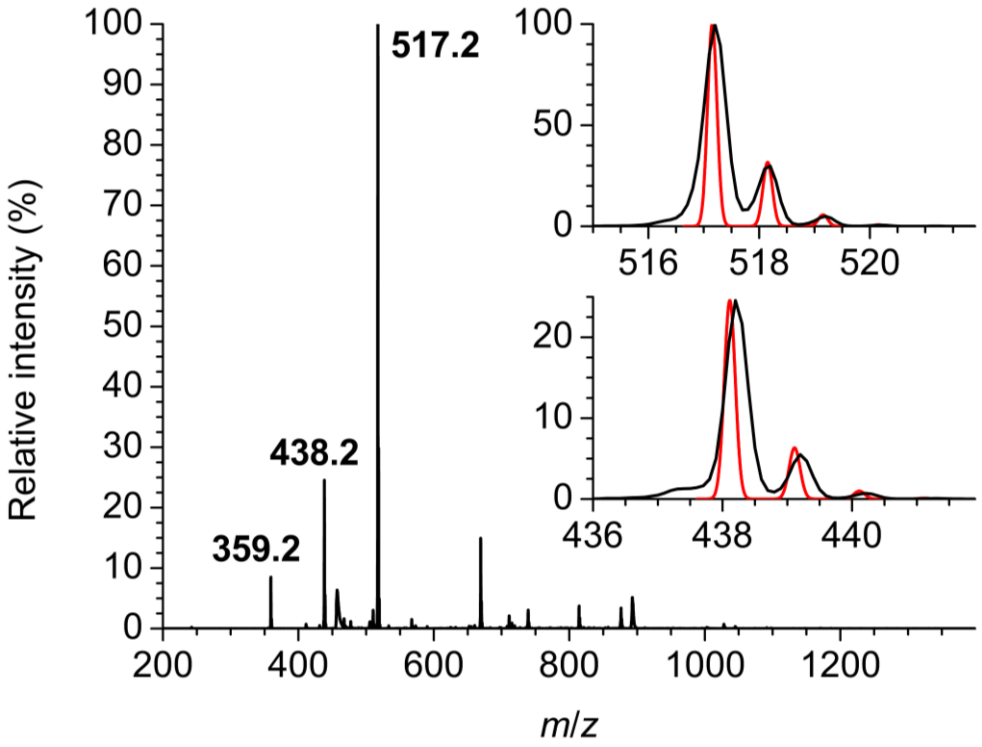

Figure S36. ESI-MS spectrum of **1** after the addition of 2 molar equivalents of py (direct infusion, THF, positive-ion mode). The inset shows the experimental (black line) and simulated (red line) isotopic patterns of the peaks at m/z = 517.2 ($[Co(bdhb)(py)_2]^+$) and 438.2 ($[Co(bdhb)(py)]^+$).

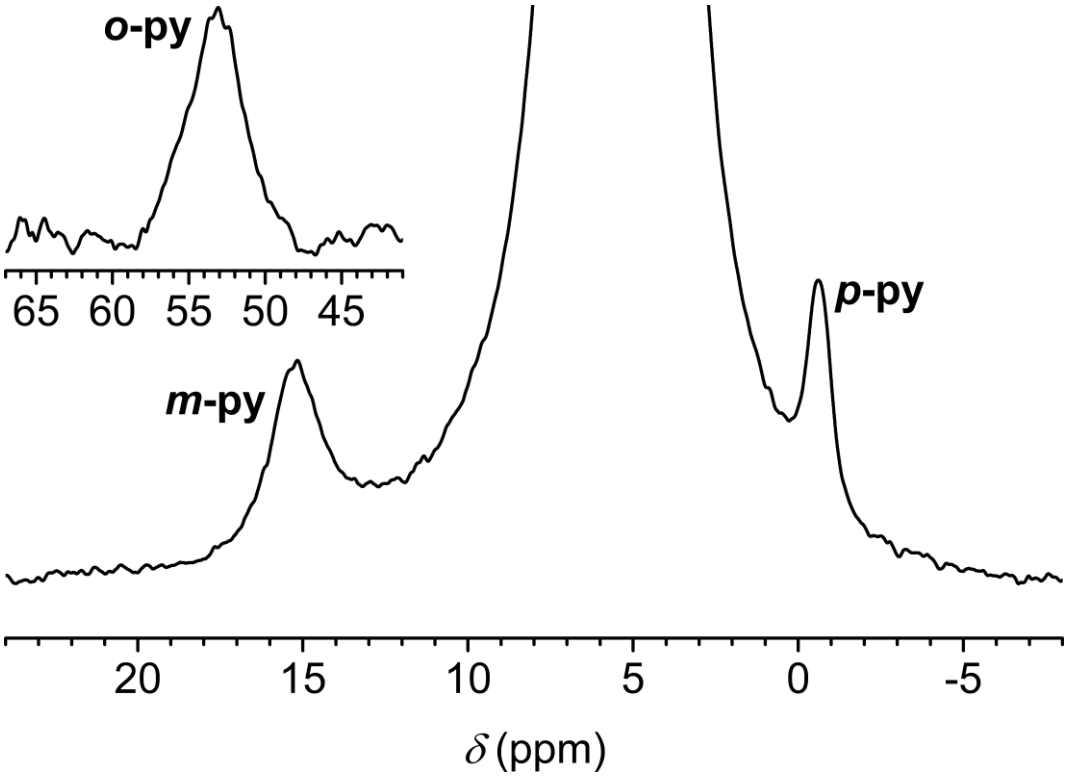

Figure S37. ^{2}H NMR spectrum of **2-*d*$_{20}$** in CD_2Cl_2 (61.42 MHz, 298 K); δ (ppm) = 5.32 (s, CD_2Cl_2). Processing parameters [TopSpin 4.3.0[1]]: SI = TD, LB = 10.00 (main panel) and 30.00 Hz (inset).

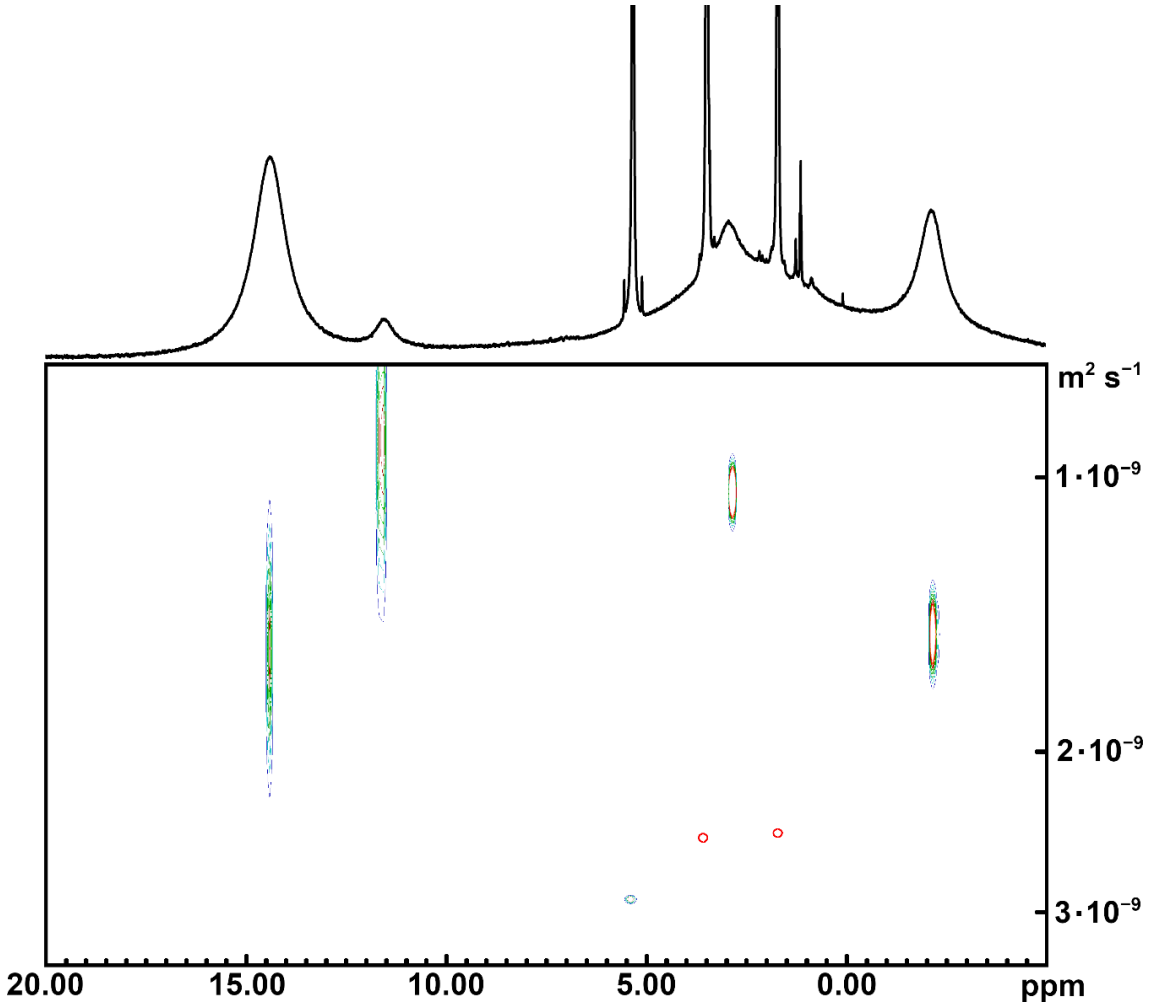

Figure S38. ^{1}H DOSY spectrum of **2** in CD_2Cl_2 (400.13 MHz, 298 K); δ (ppm) = 5.32 (residual protons in CD_2Cl_2), 3.47 [m, THF, CH_2(2,5)], 3.41 (q, Et_2O, CH_2), 1.70 [m, THF, CH_2(3,4)], 1.26 (br, pump oil, CH_2), 1.13 (t, Et_2O, CH_3), 0.86 (br, pump oil, CH_3); processing parameters [TopSpin 4.3.0[32]]: SI = 2·TD, LB = 2.00 Hz.

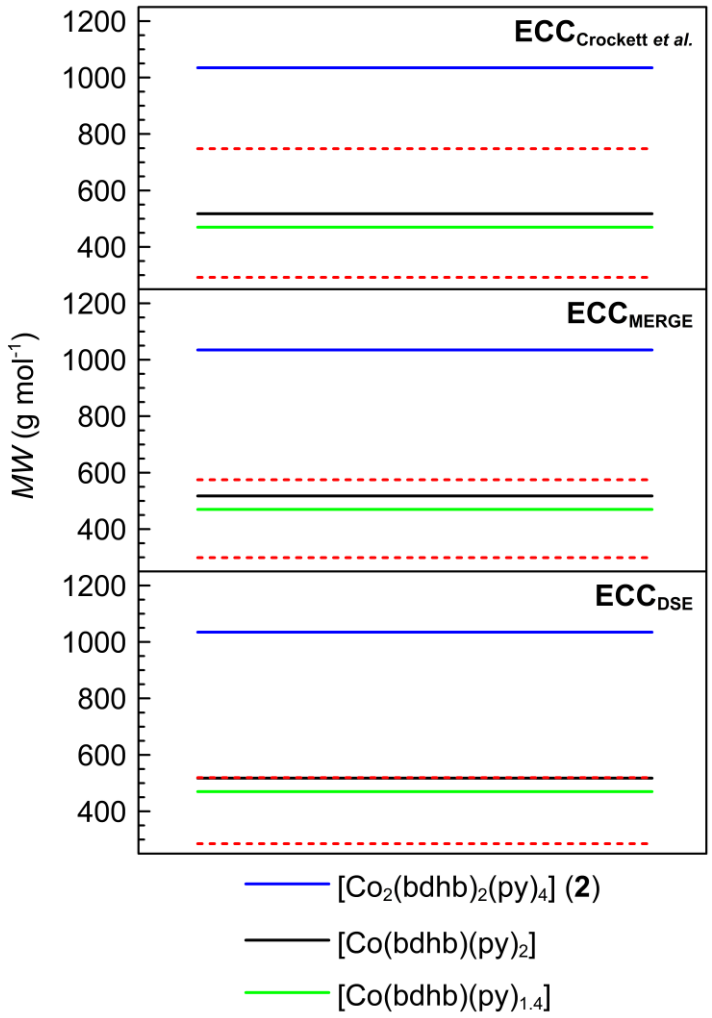

Figure S39. Graphical representation of estimated and calculated *MW*s. The dashed red lines represent the upper and lower limits of estimated *MW*s using each ECC (parameters for ECC_{DSE} and ECC_{MERGE} were taken from Ref. [6] while $ECC_{Crockett\ et\ al.}$ is the external calibration curve reported in Ref. [7]). The blue, black, and green lines represent the calculated *MW*s of dimeric **2**, monomeric $[Co(bdhb)(py)_2]$, and monomeric $[Co(bdhb)(py)_{1.4}]$, respectively.

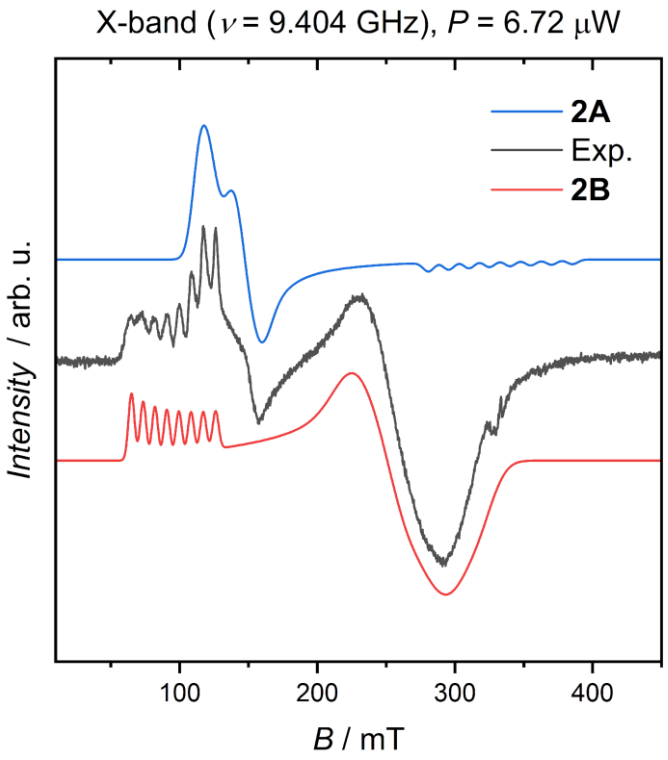

Figure S40. Experimental CW-EPR spectrum of a frozen 0.1 mM solution of **2** in CH_2Cl_2/toluene (1:1 v/v) at 10 K together with the spectral contributions denoted as **2A** and **2B**.

Table S8. NEVPT2 calculated principal components of the **g'** tensor ($g'_1 < g'_2 < g'_3$) for the ground KD of [Co(bdhb)], [Co(bdhb)(py)], *cis*-[Co(bdhb)(py)$_2$], and *trans*-[Co(bdhb)(py)$_2$] in their most stable conformers (standard Gibbs free energy window of 1 kcal mol^{-1}), as resulting from DFT geometry optimization at the B97-3c level. The experimental values for a powder sample of **2** and for components **2A** and **2B** in the frozen solution spectrum are also quoted for comparison.

	[Co(bdhb)]	[Co(bdhb)(py)]			*cis*-[Co(bdhb)(py)$_2$]				*trans*-[Co(bdhb)(py)$_2$]		**2**[b]	**2A**[c]	**2B**[c]
$\Delta G°$ [a]	0.00	0.37	0.00	0.11	0.16	0.00	0.66	0.13	0.42	0.00	–	–	–
g'_1	0.227	1.585	1.593	1.905	2.321	2.568	2.159	2.733	2.034	1.938	2.00(5)	2.010(5)	2.300(2)
g'_2	0.233	2.261	2.252	2.024	3.213	3.227	3.472	3.821	5.015	3.937	4.55(5)	4.450(5)	2.570(2)
g'_3	7.222	6.606	6.803	8.184	6.847	6.861	6.570	6.241	5.217	6.261	5.75(5)	5.650(5)	6.980(2)

[a]Calculated standard Gibbs free energy gap (in kcal mol^{-1}) from the most stable conformer of each compound (highlighted in orange). [b]Powder sample. [c]Frozen 0.1 mM solution in CH_2Cl_2/toluene (1:1 v/v).

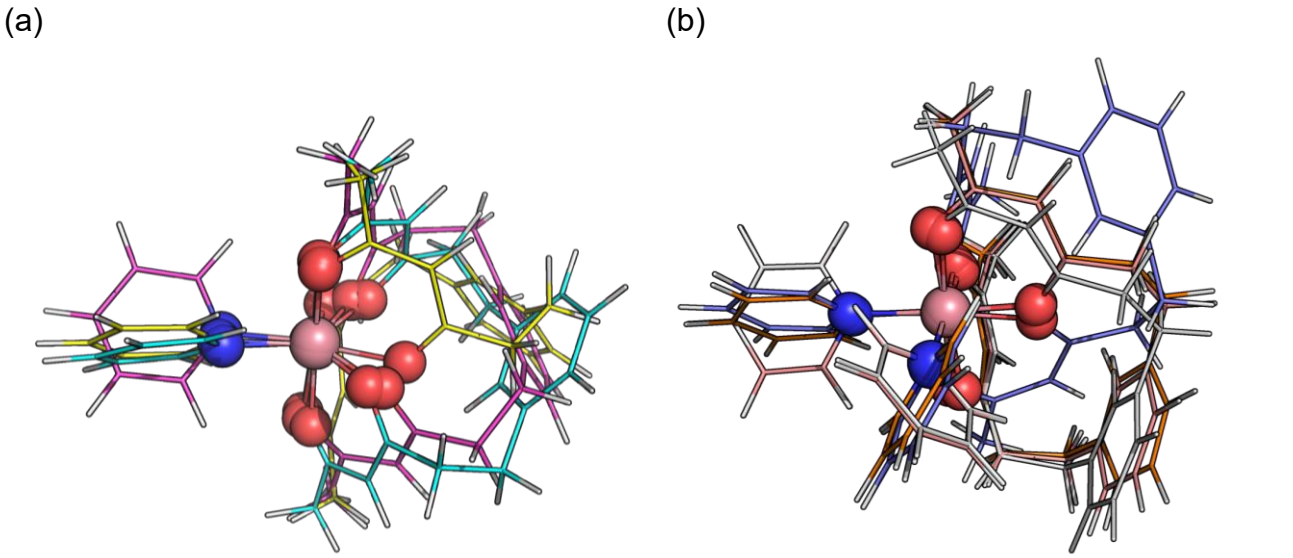

Figure S41. Superposition of the DFT geometries optimized at the B97-3c level for the lowest Gibbs free energy conformers of [Co(bdhb)(py)] (a) and *cis*-[Co(bdhb)(py)$_2$] (b), highlighting the larger differences within [Co(bdhb)(py)] vs. *cis*-[Co(bdhb)(py)$_2$] conformers.

1 *TopSpin 4.3.0*, Bruker AXS Inc., Madison, WI, USA, 2023.

2 K. S. Cole and R. H. Cole, *J. Chem. Phys.*, 1941, **9**, 341–351.

3 D. Gatteschi, R. Sessoli and J. Villain, *Molecular Nanomagnets*, Oxford University Press, Oxford, UK, 2006.

4 A. L. Pellegrino, C. Mezzalira, F. Mazzer, L. Cadi Tazi, A. Caneschi, D. Gatteschi, I. L. Fragalà, A. Speghini, L. Sorace and G. Malandrino, *Inorg. Chim. Acta*, 2022, **535**, 120851.

5 S. Stoll and A. Schweiger, *J. Magn. Reson.*, 2006, **178**, 42–55.

6 S. Bachmann, R. Neufeld, M. Dzemski and D. Stalke, *Chem. Eur. J.*, 2016, **22**, 8462–8465.

7 M. P. Crockett, H. Zhang, C. M. Thomas and J. A. Byers, *Chem. Commun.*, 2019, **55**, 14426–14429.